Reduction in the Tropical High Cloud Fraction in Response to an Indirect Weakening of the Hadley Cell

S. R. Monisha Natchiar[1], Mark J Webb[2], Francis Hugo Lambert[1], Geoffrey K Vallis[1], Cyril Julien Morcrette[3], Christopher E Holloway[4], and Denis Sergeev[1]

[1]University of Exeter
[2]UK Met Office Hadley Centre
[3]Met Office
[4]University of Reading, UK

September 11, 2023

Abstract

Tropical high cloud cover decreases with surface warming in most general circulation models. This reduction, according to the "stability-iris" hypothesis, is thermodynamically controlled and linked to a decrease in the radiatively-driven clear-sky convergence, when the peak anvil clouds rise because of the rising isotherms. The influence of the large-scale dynamical changes on the tropical high cloud fraction remains difficult to disentangle from the local thermodynamic influence, given that the mean meridional circulation remains inextricably tied to the local thermodynamic structure of the atmosphere. However, using idealized general circulation model (GCM) simulations, we propose a novel method to segregate the dynamical impact from the thermodynamic impact on the tropical high cloud fraction. To this end, our investigation primarily focuses on the mechanisms underpinning changes in the high cloud cover in the deep tropics in response to extratropical surface warming, when tropical sea surface temperatures remain invariant. We find that the relative importance of the net convective detrainment of ice cloud condensates to the cloud microphysical processes, such as the net depositional growth of ice aggregates, in controlling the tropical high cloud fraction is altitude-dependent.

Reduction in the Tropical High Cloud Fraction in Response to an Indirect Weakening of the Hadley Cell

S. R. Monisha Natchiar[1], Mark J Webb[2], F Hugo Lambert[1], Geoffrey K Vallis[1], Cyril J Morcrette[1,2], Christopher E. Holloway[3], Denis E. Sergeev[4]

[1]Department of Mathematics and Statistics, University of Exeter, Exeter EX4 4QE, UK
[2]Met Office, FitzRoy Road, Exeter, EX1 3PB, UK
[3]Department of Meteorology, University of Reading, Reading RG6 6BB, UK
[4]Department of Physics and Astronomy, University of Exeter, Exeter, EX4 4QL, UK

Key Points:

- An indirect weakening of the Hadley circulation decreases the convectively-detrained ice cloud condensates in the deep tropics
- A concurrent reduction in the net vertical transport of water vapor limits the net depositional growth of ice cloud condensates
- The relative influence of net depositional growth to net convective detrainment on the tropical high cloud response is altitude-dependent

Corresponding author: S. R. Monisha Natchiar, `m.subbiah-renganathan@exeter.ac.uk`

Abstract

Tropical high cloud cover decreases with surface warming in most general circulation models. This reduction, according to the "stability-iris" hypothesis, is thermodynamically controlled and linked to a decrease in the radiatively-driven clear-sky convergence, when the peak anvil clouds rise because of the rising isotherms. The influence of the large-scale dynamical changes on the tropical high cloud fraction remains difficult to disentangle from the local thermodynamic influence, given that the mean meridional circulation remains inextricably tied to the local thermodynamic structure of the atmosphere. However, using idealized general circulation model (GCM) simulations, we propose a novel method to segregate the dynamical impact from the thermodynamic impact on the tropical high cloud fraction. To this end, our investigation primarily focuses on the mechanisms underpinning changes in the high cloud cover in the deep tropics in response to extratropical surface warming, when tropical sea surface temperatures remain invariant. We find that the relative importance of the net convective detrainment of ice cloud condensates to the cloud microphysical processes, such as the net depositional growth of ice aggregates, in controlling the tropical high cloud fraction is altitude-dependent.

Plain Language Summary

The cloud feedback associated with changes in the tropical high cloud cover is one of the major uncertainties in calculating the current estimates of climate sensitivity, which is a measure of how much the Earth's average surface temperature would increase if we double the amount of atmospheric carbon dioxide. When the surface becomes warmer in the tropics, the tropical high cloud cover decreases. However, this raises an important question: how do circulation changes independent of the temperature changes within the tropics impact the tropical high cloud cover? Using idealized general circulation model simulations, we found that the tropical high cloud fraction decreases as a result of circulation changes induced by extratropical warming, even when the tropical sea surface temperatures are held constant. Both convective and cloud microphysical processes play significant roles in controlling the tropical high cloud fraction, and their relative importance varies with altitude. Understanding the different factors responsible for the changes in high cloud cover is important, as the area covered by these tropical high clouds can affect how much the Earth warms under climate change.

1 Introduction

Understanding the mechanisms that control the fractional coverage of tropical anvil clouds is crucial for improving estimates of Earth's climate sensitivity (Sherwood et al., 2020). The net cloud radiative effect of tropical anvil clouds formed from detrained cloud condensates of deep convective cores is approximately zero because of their counterbalancing shortwave (cloud albedo effect) and longwave effects (cloud greenhouse effect) (Hartmann & Berry, 2017). Nonetheless, the shortwave and longwave cloud radiative effects of these clouds are individually large (Ramanathan et al., 1989; Harrison et al., 1990); even small changes in the characteristics of these clouds, such as their areal extent, can have a significant impact on their radiative feedback with warming (Sherwood et al., 2020).

Tropical high cloud cover is projected to decrease with surface warming in the tropics (i.e., local warming), following the same fundamental thermodynamic principle that governs the peak height of the tropical anvil clouds, known as the Fixed Anvil Temperature or FAT hypothesis (Hartmann & Larson, 2002; Kuang & Hartmann, 2007). As surface warming causes isotherms to rise, the altitude at which maximum convective detrainment or the peak of anvil cloud fraction occurs is also predicted to increase (Zelinka & Hartmann, 2010, 2011). This upward shift of high clouds to a more stable region of the atmosphere[1] is expected to result in a reduction of the high cloud fraction, as per the stability-iris hypothesis (Zelinka & Hartmann, 2011; Bony et al., 2016). This mechanism arising out of thermodynamic constraints in the clear-sky region links the deep tropical high cloud changes to the changes in the radiatively-driven clear-sky convergence or upper-tropospheric dry static stability.

It is widely acknowledged that local surface warming (e.g., within the tropics), such as that caused by an increase in the concentration of greenhouse gases, is associated with an increase in the dry static stability (Knutson & Manabe, 1995). Evaluating this within the framework of the dry static energy budget (see equation (B1)) would indicate that the subsidence velocity tends to decrease, as the dry static stability increases without a commensurate increase in the rate of radiative cooling within the subsidence regions[2]. Additionally, the absence of unreasonably large increases in latent heating in the tropical ascent regions, along with the decrease in subsidence velocity, implies a weakening of the tropical mean circulation with local surface warming (refer to equation 9 of Jenney et al. (2020)). This in turn implies a reduction in the tropical convective mass flux (Jeevanjee, 2022). However, there is very limited insight into how changes in the circulation without the attendant temperature changes influence the high cloud changes in the deep tropics, given that the large-scale mean meridional (or Hadley) circulation is thermally direct and remains inextricably tied to the thermodynamic structure of the atmosphere.

To isolate the large-scale circulation (i.e., Hadley cell) changes from the thermodynamic changes in the tropics, we choose to warm the extratropics, keeping the tropical sea surface temperatures unchanged, and analyze their impact on the tropical high cloud fraction. The importance of subtropical eddy momentum and/or eddy energy fluxes in determining the strength of the Hadley cell has been explored in a number of studies, including Bordoni and Schneider (2008); Singh and Kuang (2016); Singh et al. (2017); Kim et al. (2022) and the references therein. However, there remains a paucity of studies that focus on the tropical cloud changes caused by eddy-induced changes in the mean meridional circulation. This study will focus on the changes in the tropical high cloud fraction caused by changes in the mean meridional circulation owing to extratropical surface warming, while the tropical sea surface temperatures remain unchanged.

Some of the questions we aim to address in this study are: does the peak of tropical anvil clouds shift to higher altitudes in response to changes in the atmospheric dynamics induced by extratropical surface warming, resulting in an increase in the upper-tropospheric static stability? In the absence of a significant free-tropospheric temperature increase in the tropics in response to extratropical warming, what governs the changes in the peak anvil cloud fraction? Given the decrease in the meridional temperature gradient, we expect a weakening of the Hadley circulation by the large-scale extratropical eddies. Does a weakened Hadley cell then cause a reduction in the tropical high cloud fraction by modulating the tropical convective mass flux?

Moreover, while the stability-iris hypothesis (Bony et al., 2016) suggests that the changes in the upper-tropospheric dry static stability play a primary role in determining changes in the high cloud fraction, the impact of cloud microphysical processes (among other factors) on the extent of high clouds in climate change scenarios remains less explored. Even with the stability-iris hypothesis finding some observational support (Saint-Lu et al., 2020), there are some modeling studies (Tsushima et al., 2014; Singh & O'Gorman, 2015; Chen et al., 2016; Ohno & Satoh, 2018; Ohno et al., 2019), and approximately one-third of the cloud-resolving models within the RCEMIP framework (Wing et al., 2020; Stauffer & Wing, 2022) that predict an expansion in the anvil cloud area with warm-

[1] Rising of tropical high clouds to a lower atmospheric pressure level results in an increased saturation specific humidity at a fixed temperature, thereby increasing its static stability.

[2] With the assumption that the change in the evaporative cooling rate remains negligible.

ing. Consequently, the relative importance of cloud microphysical processes in influencing the tropical high cloud coverage remains unclear.

More recently, Seeley et al. (2019) and Beydoun et al. (2021) have included sinks of ice cloud condensates as important terms in predicting cloud lifetime and therefore the anvil cloud fraction. Sinks of cloud condensates via precipitation, evaporation or sublimation and dilution or entrainment-mixing were found to be important in the accurate determination of the anvil cloud fraction. Seeley et al. (2019) defined anvil cloud fraction as the product of gross detrainment and a positive-definite cloud lifetime, emphasizing the significance of cloud microphysical timescales in determining the anvil cloud fraction. Using their diagnostic framework, Beydoun et al. (2021) further corroborated that both detrainment and cloud lifetime are crucial for accurately predicting anvil cloud coverage. The role of cloud microphysical processes in determining anvil cloud fraction was also demonstrated in cloud-resolving simulations run in radiative-convective equilibrium using both a simple and a complex microphysics scheme (Jeevanjee, 2022). The study found that identical clear-sky convergence peaks did not yield similar anvil cloud fractions, attributing this discrepancy to variations in the microphysics schemes.

Although incorporating a parameter that quantifies cloud decay is important for the accurate determination of anvil cloud lifetimes and therefore anvil cloud fraction as suggested in these studies, not much importance has been placed on microphysical *sources* of ice cloud condensates, such as the net depositional growth of ice cloud condensates, which is one focus of our study. Cloud ice mixing ratio that affects the anvil cloud lifetime has been found to be largely influenced by the net convective detrainment but also by the depositional growth of ice cloud condensates (Gasparini et al., 2021).

Addressing the question of how tropical high clouds' areal extent responds to circulation changes induced by non-local surface warming is also especially relevant because of arctic amplification (Manabe & Stouffer, 1980), where the arctic is warming at more than twice the global rate over the past 50 years (Holland & Bitz, 2003; Davy et al., 2018). Essentially, understanding the interplay between convective, advective and cloud microphysical processes in controlling the tropical anvil cloud fraction in GCMs is vital to constrain the "tropical anvil cloud area feedback", which is a major source of uncertainty in the estimation of equilibrium climate sensitivity.

This paper is organized as follows. Section 2 describes the model configuration used in this study, while section 3 delves into the results, with the weakening of the Hadley circulation caused by extratropical surface warming explored in sub-section 3.1, and the two pathways leading to the reduction in the high cloud fraction investigated in sub-section 3.2. The paper ends with the discussion and conclusions presented in section 4.

2 Model configuration: aquaplanet simulations with prescribed SSTs

Idealized aquaplanet simulations are performed using the Global Atmosphere 7.0 configuration of the Met Office Unified Model (UM) (Walters et al., 2019) in an atmosphere-only General Circulation Model (GCM) setup with prescribed sea surface temperatures. The model employs a semi-implicit, semi-Lagrangian formulation to solve the three-dimensional non-hydrostatic, compressible equations of motion, and utilizes physical parameterizations to represent subgrid-scale processes such as atmospheric radiation, boundary-layer turbulence, convection, clouds, and precipitation. The model setup employs a single-moment microphysics scheme as described in Walters et al. (2019) that is primarily based on a modified Wilson and Ballard (1999) microphysics scheme. Here, only the mass mixing ratio of the hydrometeor species is determined prognostically, while the number concentration of the respective hydrometeor species is diagnosed. The model takes into account only one type of ice species, *viz.*, ice aggregates, excluding the other forms such as ice crystals, snow, and graupel. The calculation of microphysical transfer rates between the ice species (aggregates) and other water species uses generic ice particle size distribution from Field et al. (2007). Furthermore, a mass-flux convective parameterization scheme (Gregory & Rowntree, 1990) with adaptive detrainment (Derbyshire et al., 2011) and a CAPE-based closure is employed. Clouds are parameterized using either a prognostic (PC2 cloud scheme; Wilson et al. (2008)) or a diagnostic scheme (the Smith cloud scheme; Smith (1990)).

The model equations are integrated over a period of 20 years, with a horizontal resolution of 2.5° longitude by 2° latitude, and with 38 vertical levels between the surface and the model top at 40 km. The integration time step is fixed at 20 minutes. Monthly mean diagnostics are output at regular intervals. The last 15 years of simulation data are analyzed, discounting the initial 5 years to account for the spin-up period. More details on the model physics and parameterization schemes can be found in Boutle et al. (2017) and Walters et al. (2019).

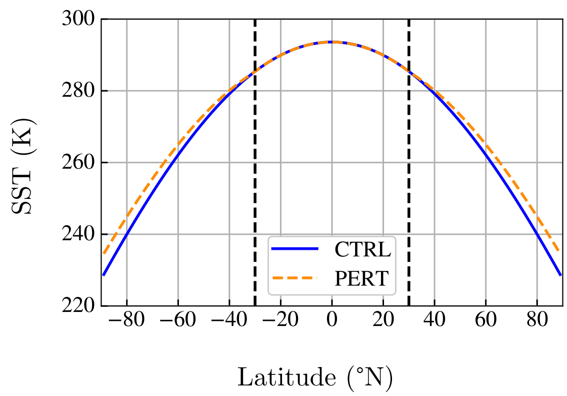

Figure 1: Prescribed zonal-mean sea surface temperatures in control (blue solid) and perturbed (orange dashed) aquaplanet simulations using the UM. The sea surface temperatures remain unchanged in the tropics (between ±30°N latitudes).

Both the control (CTRL in figure 1) and perturbed (PERT) simulations are forced with prescribed sea surface temperatures (SSTs) that spatially vary only along the meridional direction. The control SSTs are obtained from the steady-state zonal-mean SSTs of a 20-year simulation with a slab-ocean that are smoothed meridionally using a Gaussian kernel. Here, the slab-ocean has a heat capacity of $1{\times}10^7\,\mathrm{J\,K^{-1}\,m^{-2}}$, corresponding to a slab ocean depth of approximately 2.5 m. The CO_2 concentration is fixed at 594.1 ppm by weight. In the case of perturbed simulations (PERT), SSTs remain identical to the CTRL within the latitudinal bounds of ±30°N. Beyond these bounds in the extratropics (extending from ±30°to ±90°N), the increase in SSTs is linear as prescribed by $\Delta T = m\Delta\theta$, with $\Delta\theta$ denoting the latitudinal difference from 30° (i.e., $\Delta\theta = |\theta| - 30°$) and m representing the slope of linear increase set at 0.1 K per degree. This leads to a warming of 6 K at each pole. The model excludes any seasonality or sea ice components.

3 Results

3.1 Weakening of the Hadley circulation

The weakening of the Hadley circulation is depicted by the changes in the mass meridional stream function between the perturbed and control climates (i.e., $\psi_{PERT} - \psi_{CTRL}$), as shown in color in figure 2. The corresponding stream function in the control climate is delineated using black curves. Regardless of whether a prognostic (panel a) or diagnostic cloud scheme (panel b) is used, the mean mass meridional circulation exhibits a comparable degree of weakening of at least 5% in the tropical mid-troposphere.

Our investigation is focused on the tropical ascent region, specifically between altitudes 8 and 12.5 km (i.e., the upper troposphere). We observe insignificant changes in the time-averaged fractional area of ascent within the tropics (determined using vertical velocity at 500 hPa). This result is apparently inconsistent with previous research by Schiro et al. (2019) and Jenney et al. (2020). However, it should be noted that Schiro et al. (2019) and Jenney et al. (2020) reported changes in the fractional area of ascent and/or high cloud fraction in response to *local* warming and not due to remote or extratropical warming as in the present study. This study predominantly aims to decipher the cause for the reduction in the high cloud fraction that is observed in the tropical ascent region or the deep tropics[3], in light of the observed weakening of the Hadley circulation due to extratropical warming.

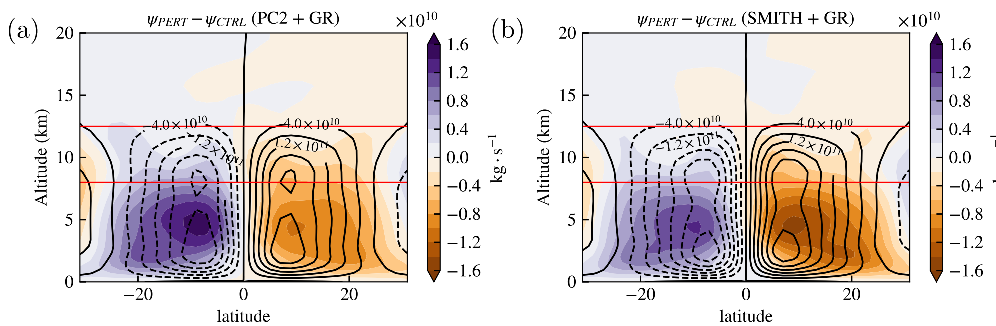

Figure 2: The imposed extratropical surface warming (not shown here) causes a weakening of the large-scale Hadley circulation, depicted here via a difference in the mass meridional stream function (ψ) between the perturbed and control climates (in color). Note that the latitude range shown is between ±30°N. The black contours represent ψ_{CTRL} with a contour spacing of 4×10^{10} kg · s^{-1}. Simulations are run with either a prognostic (PC2; panel a) or a diagnostic (Smith; panel b) cloud scheme, and a mass-flux convection scheme. A maximum Hadley cell weakening at 500 hPa is approximately 7% in simulations with the PC2 cloud scheme (panel a), and approximately 5% using the Smith scheme (panel b). The region of interest is demarcated by horizontal red lines at 8 and 12.5 km.

Our analysis reveals a decrease in the boundary layer specific humidity in the tropics as a result of extratropical warming (as shown in panels e, f of figure 3 focusing on the tropics between latitudes ±30°N), which can be attributed to the lower branch of the Hadley circulation transporting reduced amounts of moisture into the deep tropics due to the weakened mean circulation (refer to supplementary figure S1). This reduced influx of moisture subsequently leads to a decrease in the relative humidity within the region (panels c, d of figure 3), notwithstanding a slight reduction in the free-tropospheric temperature (panels g, h of figure 3).

The decrease in the free-tropospheric tropical temperature can be understood as a direct consequence of the tropical temperature profile adhering to a moist adiabat, thus conforming to a cooler moist adiabat in response to a reduced boundary layer equiva-

[3] Note that the terms "tropical ascent region" and "deep tropics" will be used interchangeably throughout the manuscript.

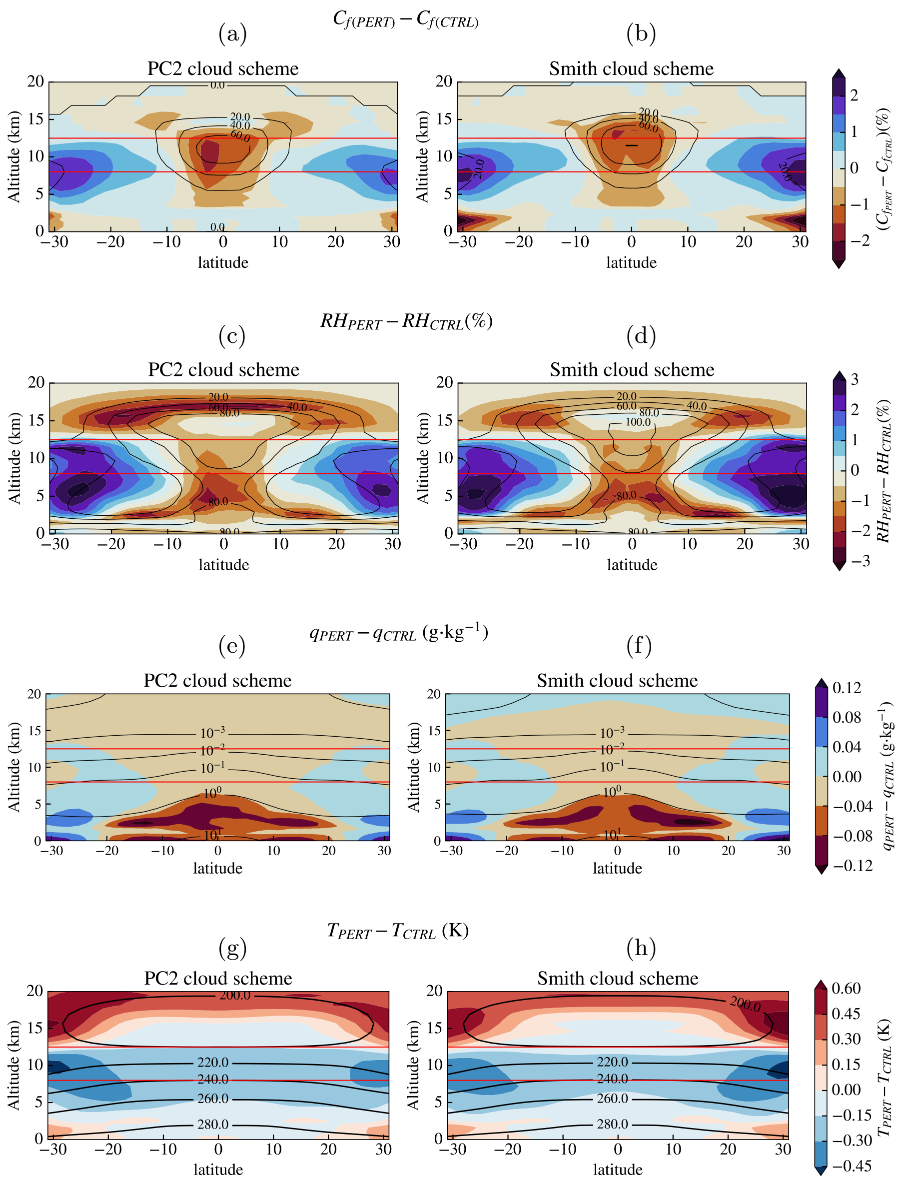

Figure 3: Contour plots showing responses of ice cloud fraction (C_f), relative humidity (RH), specific humidity (q), and air temperature (T) in the tropics (i.e. between ±30°N) to imposed extratropical surface warming (as shown in figure 1). Control climate is represented using black contours and the response is shown in color. Sub-figures (a,b) depict at least a 1% reduction in C_f in the tropical ascent region, which corresponds to a decrease in RH (c,d) and q (e,f) in the same region (between ±7°N), albeit a slight cooling of the mid- to upper troposphere (g,h). Simulations are run with a mass-flux (Gregory-Rowntree) convection scheme, and with either a prognostic (PC2; left panel) or diagnostic (Smith; right panel) cloud scheme.

lent potential temperature. The reduction in high cloud fraction (panels a, b of figure 3) aligns with a decrease in the relative humidity (panels c and d), and as will be shown in figure 5, a decrease in the mass fraction of ice cloud condensates within the region. In the next section, we investigate the underlying mechanisms behind this relationship.

3.2 Mechanisms underpinning the reduction in high cloud fraction

We examine the causes for the decrease in high cloud fraction within the deep tropics, employing two distinct physical pathways as outlined in figure 4. Pathway I (in purple) illustrates the decrease in ice cloud fraction due to the reduced detrainment of ice cloud condensates resulting from a weakened Hadley circulation, while Pathway II (in green) details the reduction of ice cloud fraction caused by a decrease in the net depositional growth of ice cloud condensates. Both pathways lead to a decrease in the ice cloud condensates in the upper troposphere resulting in a decline in the high cloud fraction in the tropical ascent region (refer to figure 5 which shows a high correlation in terms of both Pearson (r) and distance correlation (r_D) coefficients between changes in the mass fraction of ice cloud condensates and ice cloud fraction in the tropical upper troposphere; note that the distance correlation coefficient (Székely et al., 2007; Chaudhuri & Hu, 2019)[4] is a non-linear correlation metric between any two random variables, without strict assumptions about their distributions. It is more robust than Pearson correlation, which assumes normality and can only quantify linear relationships). In the following subsections, we describe Pathway I (section 3.2.1) and Pathway II (section 3.2.2) in more detail.

3.2.1 Pathway I or Convective Pathway: Decrease in the net detrainment of ice cloud condensates

Pathway I for the decrease in high cloud fraction is investigated through figures 6 to 9. Both physical pathways are premised on the understanding that extratropical warming causes a weakening of the mean meridional circulation. Based on the principles of mass conservation, and given the negligible changes in the subsidence (or ascent) area fraction within the tropics, it follows that there is a corresponding reduction in the convective mass flux within the region of tropical large-scale ascent (see figure 6 a,b). It is worth mentioning that although the studies conducted by Jenney et al. (2020) and Jeevanjee (2022) have yielded similar results, specifically a decrease in convective mass flux in the tropical ascent region with warming, their research focused on local surface warming, which presents a different context from our current study.

Within the region characterized by peak net detrainment and hence peak anvil cloud fraction (specifically, around altitude of 11.5 km), we observe a reduction in the net convective detrainment of mass flux (as shown in figures 6 c,d). Assuming no significant changes in the precipitation efficiency, we expect a corresponding decrease in the net detrainment of ice cloud condensates into the upper troposphere. Note that the reduction in the mass fraction of ice cloud condensates exhibits a strong correlation with that of ice cloud fraction (figure 5). Consequently, the factors influencing changes in the mass fraction of ice cloud condensates would have a significant impact on the changes in ice cloud fraction in the deep tropical upper troposphere.

A minor increase in the net detrainment of mass flux is observed between altitudes 8 and 10 km, a transitional region between net entrainment in the mid-troposphere and net detrainment in the upper troposphere (figures 6 c,d and 7). While changes in the net convective detrainment significantly impact the reduction of ice cloud fraction near the peak net detrainment region, phase change and precipitation processes become crucial between 8 and 10 km. This observation is further supported by figures 8 and 9. For in-

[4] Some important properties of the distance correlation coefficient (r_D) between any two random variables X and Y are: (1) $0 \leq r_D(X,Y) \leq 1$, (2) $r_D(X,Y) = 0$ iff X and Y are independent.

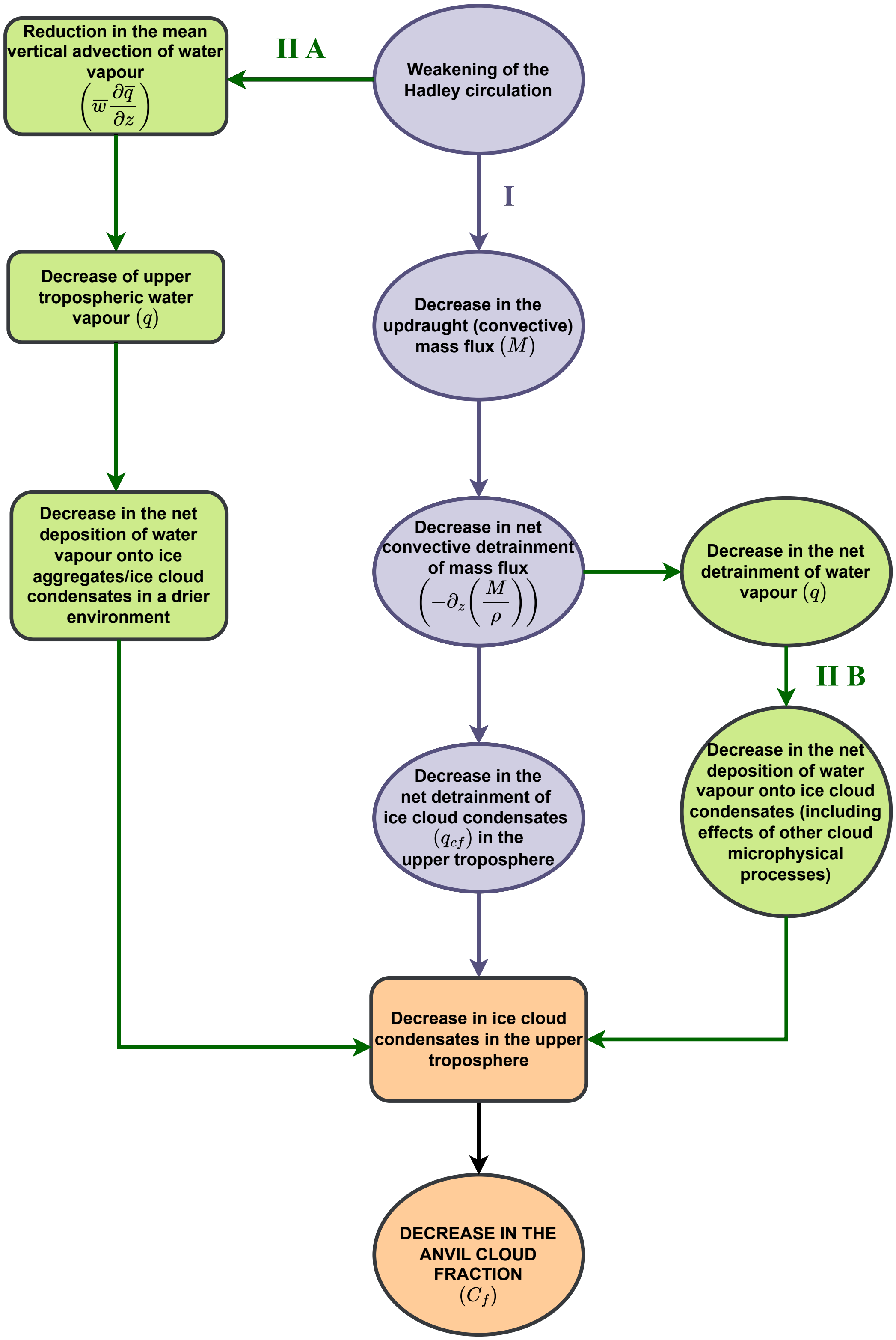

Figure 4: Schematic illustrating the causal links between high cloud reduction in the deep tropics and various environmental and cloud microphysical factors. Pathway I (purple) primarily represents the decrease in high clouds caused by reduced convective detrainment of mass flux due to a weakened Hadley circulation. Pathway II (green) highlights the dominant role of cloud microphysics, specifically the net deposition of water vapor onto ice aggregates, which in turn is linked to the mean vertical advection of water vapor ($\bar{w}\partial\bar{q}/\partial z$) (II A) and a reduced convective detrainment of water vapor (II B). For further details on the derivation of moisture convergence, refer to Appendix A.

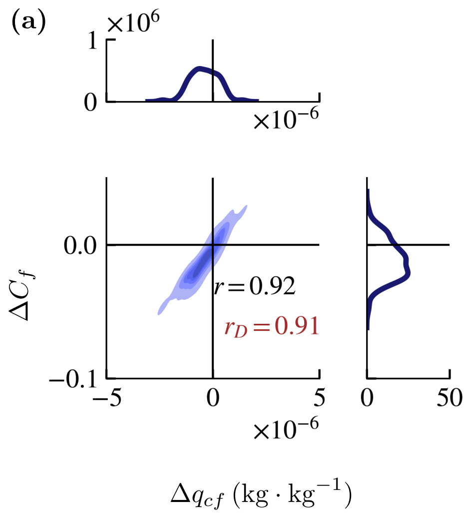

Figure 5: Kernel density estimates for the joint probability density function of the zonal and annual-mean mean changes in ice cloud fraction (ΔC_f) and the mass fraction of ice cloud condensates (Δq_{cf}) are depicted within the altitude range of 8 - 12.5 km. The corresponding Pearson ($r = 0.92$) and distance correlation coefficients ($r_D = 0.91$) reveal a strong positive correlation between ΔC_f and Δq_{cf}.

stance, figure 8 shows a strong correlation between changes in net detrainment of mass flux and ice cloud fraction near the peak net detrainment region (around 11.5 km), while the correlation is weak at the lower altitudes between 8 and 10 km. Since the convective tendency of q_{cf} takes into account the phase change and precipitation processes that are modelled within the convection scheme, it presumably increases the correlation coefficient between the changes in the convective tendency of q_{cf} and ice cloud fraction changes in the lower altitude range, as shown in figure 9. For the bulk cloud scheme formulation that includes phase change and precipitation processes, see Appendix C (specifically equation (C3) for the sum of liquid and ice condensate fluxes).

3.2.2 Pathway II or Microphysical Pathway: Importance of phase-change and precipitation processes: Decrease in the net deposition of water vapor onto ice cloud condensates

The importance of cloud microphysical processes as a source of ice cloud condensates, such as net deposition of water vapor onto ice cloud condensates, in determining the ice cloud fraction response to extratropical warming is explored in Pathway II. For comparative clarity, changes in the tendency of mass fraction of ice cloud condensates due to net deposition ($\Delta(\partial q_{cf}/\partial t)_{netdep}$) are plotted on the same horizontal scale as the tendency due to convection ($\Delta(\partial q_{cf}/\partial t)_{conv}$), against ice cloud fraction changes along the vertical axis (see figures 10 and 9, respectively). It becomes evident that between 8 and 10 km, the changes in the tendency of ice cloud condensates resulting from net deposition become comparable to those due to convection, and are strongly correlated to the changes in ice cloud fraction. It is important to note that the convective tendency of q_{cf} encompasses contributions not only from net convective detrainment but also from simple phase change and microphysical processes that are modeled within the convection scheme (see Appendix C for more details).

Upon further investigation, it becomes evident that the primary reason for the decrease in the microphysical tendency of q_{cf} attributed to net deposition is a reduction in the advective tendency of water vapor. Within the altitude range of 8 - 10 km, the decrease in water vapor advective tendency is at least 2 orders of magnitude larger than

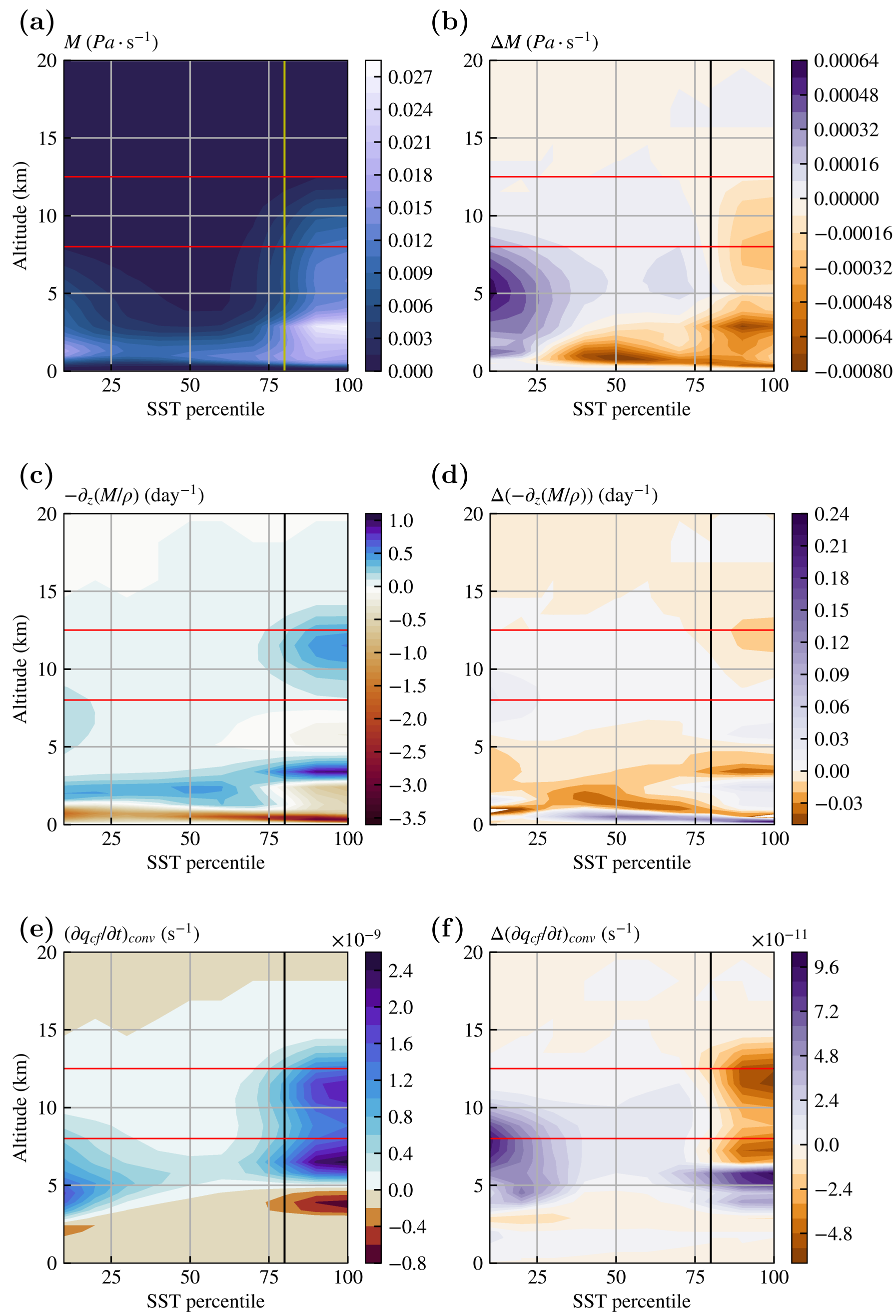

Figure 6: Binned monthly-mean data as a function of local (i.e., tropical) SST percentiles for updraft mass flux (M), net convective detrainment of mass flux ($-\partial_z(M/\rho)$), and tendency of ice cloud condensates due to convection (($\partial q_{cf}/\partial t)_{conv}$ in the control climate (subfigures a, c, e); their corresponding response values are plotted in the right panel (subfigures b, d, f). The 80th SST percentile (black vertical line) in both the control (left panel) and the response (right panel) separates the large-scale tropical ascent from the tropical descent region.

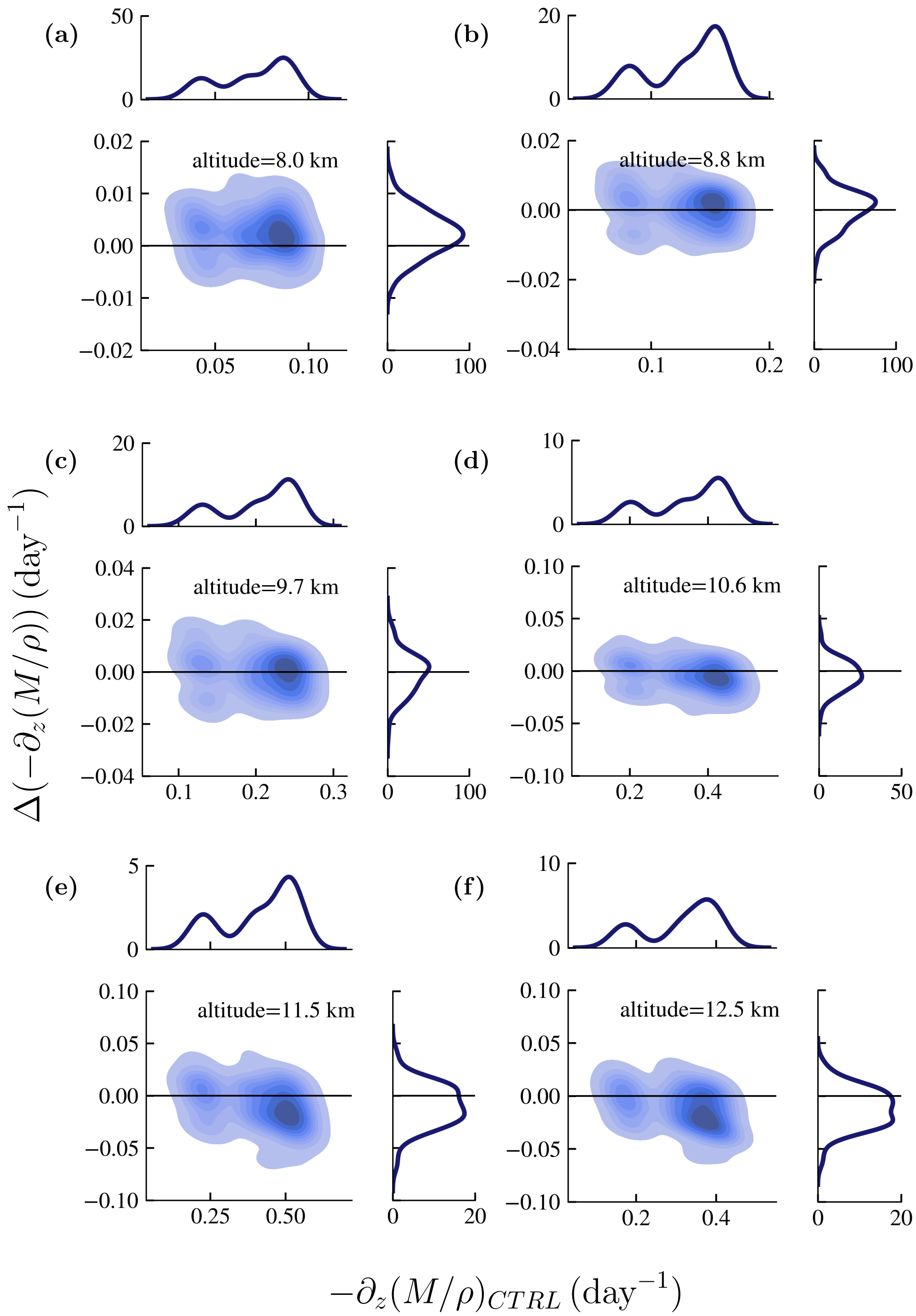

Figure 7: Kernel density estimates for the joint probability density function of the zonal- and annual-mean response of the net convective detrainment and the control are plotted for 15 simulation years. The contours represent areas with equal probability density, with the darker areas indicating higher probability density. The kernel density estimates for the marginal probability distribution of the corresponding variables are plotted in the top and the right axes of each subfigure. A decrease in the net convective detrainment of mass flux can be seen for altitudes > 10 km, where most of the net detrainment occurs.

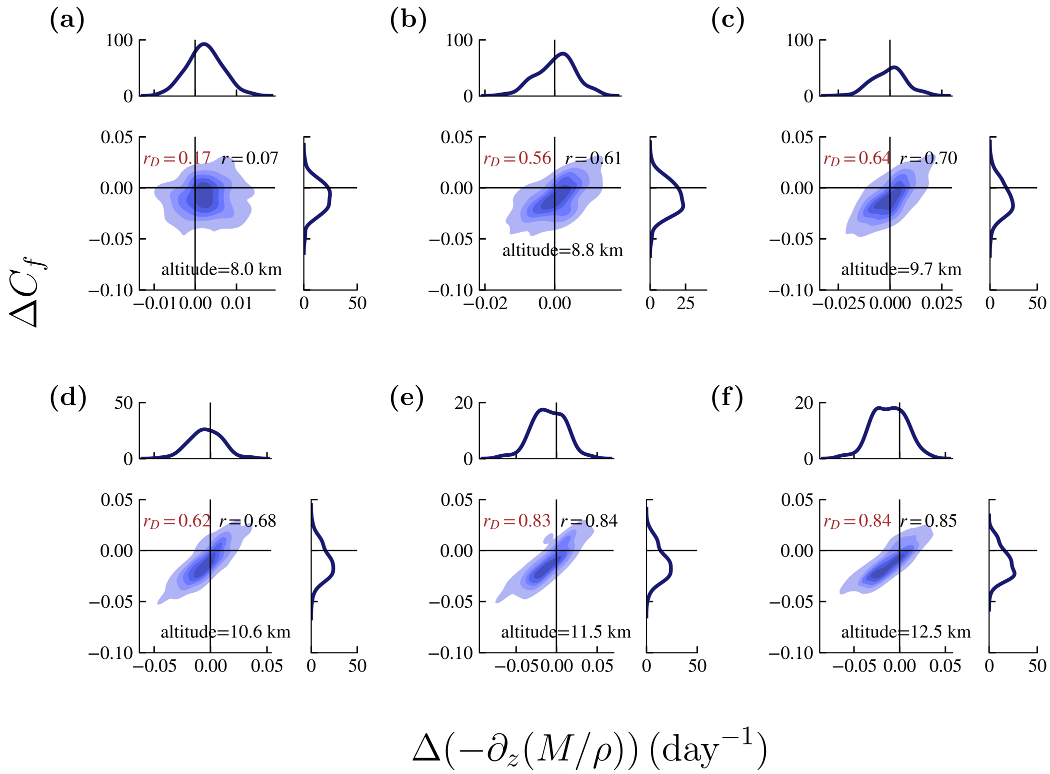

Figure 8: Kernel density estimates for the joint probability density function of the responses of ice cloud fraction (ΔC_f) and net convective detrainment of mass flux ($\Delta(-\partial_z(M/\rho))$) to extratropical warming. As in figure 7, the zonal- and annual means of the respective quantities are plotted here. The Pearson (r) and distance correlation coefficients (r_D) between ΔC_f and $\Delta(-\partial_z(M/\rho))$ increase with altitude.

at the peak net detrainment region (see figure 12). This leads to decreased mean environmental water vapor within the tropical ascent region, subsequently limiting the growth of ice cloud condensates via net water vapor deposition onto pre-existing particles. That is, a drier environment increases sublimation of ice cloud condensates to water vapor, but decreases the depositional growth of those condensates, thereby reducing their net depositional growth. The reduction in the mean vertical advection of water vapor in the upper troposphere of tropical ascent region, evident in figure 13, further corroborates the decrease in the advective tendency of water vapor within the altitude range considered.

Cloud microphysical processes play a pivotal role not only as a sink term (Seeley et al., 2019; Beydoun et al., 2021), but as has been demonstrated, also as a source term for q_{cf} within the large-scale ascent region of the tropical upper troposphere. The importance of cloud microphysical processes as a source term, primarily through net deposition, is particularly noticeable between 8 and 10 km; this altitude range serves as a transition zone between the region of net entrainment in the mid-troposphere and net detrainment in the upper troposphere. This is evident from figure 11(a) showing the net depositional tendency of q_{cf} in the control climate, and figures 10(a-c) and 11(b) that depict their response to a weakened Hadley circulation caused by extratropical warming. Additional figures illustrating the leading-order influence of the changes in the net convective detrainment on the peak high cloud fraction changes in the deep tropics are

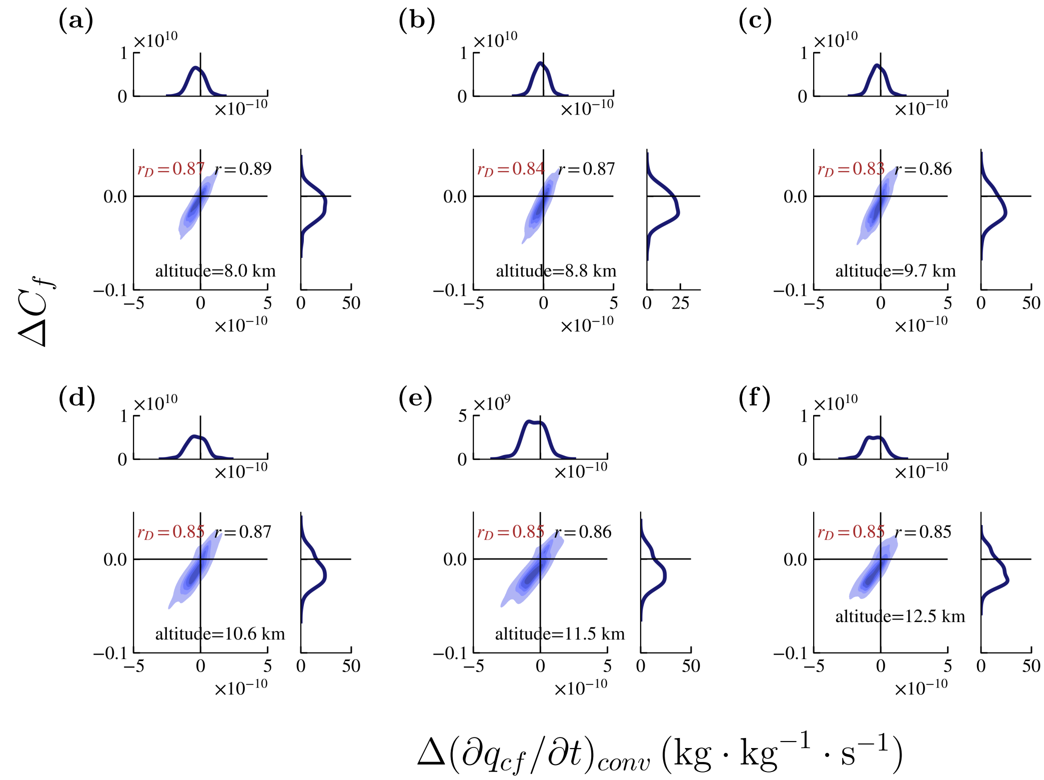

Figure 9: Kernel density estimates for the joint probability density function of the changes in ice cloud fraction (ΔC_f) and tendency of mass fraction of ice cloud condensates due to convective processes ($\Delta(\partial q_{cf}/\partial t)_{conv}$) are plotted. As in figure 7, the zonal- and annual means of the respective quantities are plotted here. The Pearson (r) and distance correlation coefficients (r_D) show a strong correlation between ΔC_f and $\Delta(\partial q_{cf}/\partial t)_{conv}$ across all the altitudes considered.

provided in the supplementary. For instance, figure S12(a,b) depicts the ratio of the changes in convective to net deposition tendencies of q_{cf} in response to extratropical warming. Similarly, the inverse ratio shown in the supplementary figure S12(c) highlights the critical contribution of cloud microphysical processes, such as the net deposition of water vapor onto ice cloud condensates, that involves the summation of vapor deposition and sublimation processes, within the altitude range of 8 to 10 km.

4 Discussion and Conclusions

Through idealized aquaplanet simulations, we have investigated the factors influencing the reduction in the fractional coverage of tropical high clouds in the large-scale ascent region, in response to an indirectly weakened Hadley circulation caused by extratropical surface warming.

Our study specifically examined the relative importance of the impact of net convective detrainment and cloud microphysical processes, with a focus on the net depositional growth of ice cloud condensates, which encompasses both deposition and sublimation processes. We have identified two key physical pathways driving changes in the tropical high cloud coverage: the first pathway involves net convective detrainment acting as the primary source of ice cloud condensates, particularly near the peak net de-

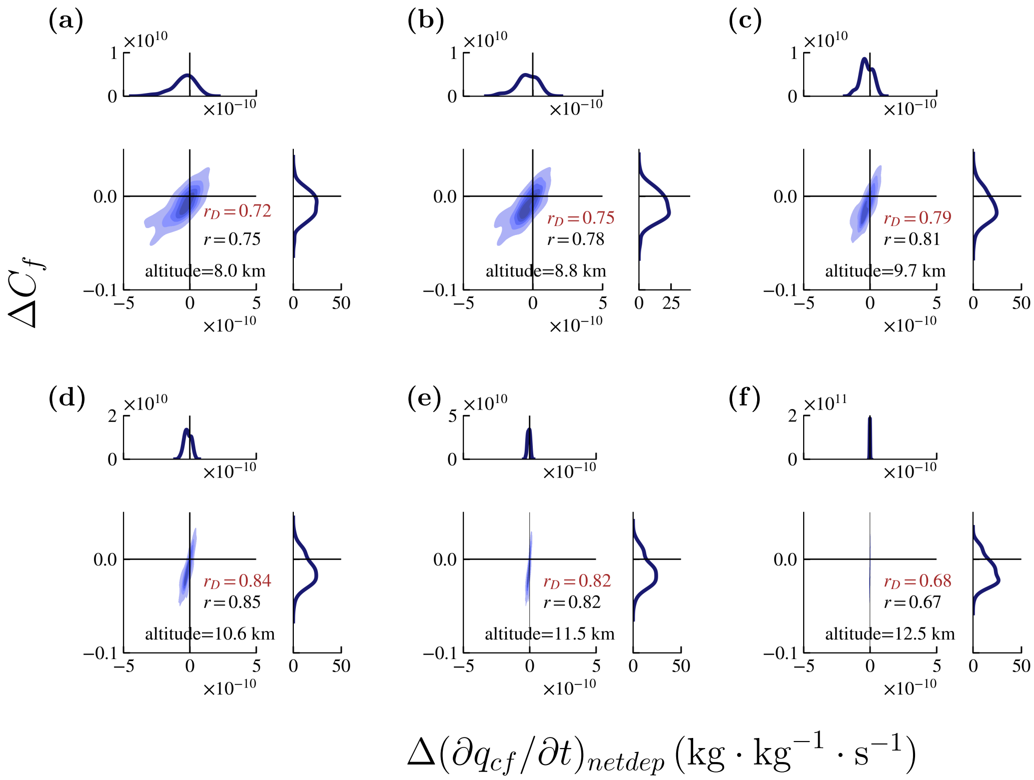

Figure 10: Kernel density estimates are used to show the joint PDF of the changes in ice cloud fraction and the tendency of mass fraction of ice cloud condensates due to net deposition of water vapor. A strong correlation between ΔC_f and $\Delta(\partial q_{cf}/\partial t)_{netdep}$ throughout the upper troposphere is evident. Particularly, the changes in $(\partial q_{cf}/\partial t)_{netdep}$ are comparable to that of $(\partial q_{cf}/\partial t)_{conv}$ in the lower end of the altitude range considered.

trainment region at around 11.5 km in the upper troposphere (pathway I), while the influence of microphysical processes, *viz.* the net deposition of water vapor onto ice cloud condensates is explored via the second pathway (pathways IIA and IIB). The influence of cloud microphysical processes is particularly significant within the altitude range of 8 to 10 km that forms the transition zone between mid-tropospheric net entrainment and upper-tropospheric net detrainment.

The stability-iris hypothesis suggests a decrease in the anvil cloud fraction with local warming, as the clouds ascend to a more stable atmosphere following the rising isotherms (Fixed Anvil Temperature or FAT hypothesis; Hartmann and Larson (2002)). When clouds ascend to lower pressure levels in these warming scenarios, they encounter a more stable environment, resulting in a reduced detrainment of moisture and condensates. While we observe increased dry static stability near the tropopause with extratropical warming (refer to supplementary figure S10), we do not observe a concomitant increase in the upper-tropospheric temperature, nor a rise in the altitude at which deep convecting clouds detrain water vapor and condensates. In contrast to the local warming scenarios, our results show a slight cooling of the upper troposphere, attributed to the adjustment of the lapse rate towards a lower moist adiabatic rate due to reduced boundary layer humidity.

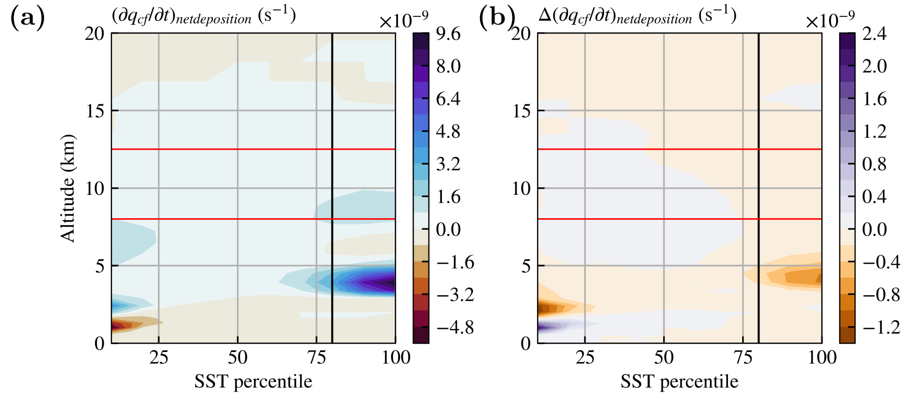

Figure 11: Binned monthly-mean data of the tendency of mass fraction of ice cloud condensates due to net deposition of water vapor ($(\partial q_{cf}/\partial t)_{netdeposition}$) as a function of local SST percentiles is presented. The 80th SST percentile separating the large-scale tropical ascent and descent regions is represented by a black vertical line in both the control (left panel) and the response (right panel). The analysis includes data from all longitudes within the tropics (±30°N) and reveals a reduction in the net deposition throughout the tropical free troposphere in the large-scale ascent region.

We ascribe the decrease in the high cloud fraction seen in our simulations (in the vicinity of the region of peak net detrainment) mainly to a decrease in the net detrainment of mass flux due to a reduced updraft mass flux. Assuming negligible changes in the precipitation efficiency accompanying the dynamical changes induced by extratropical warming, this would imply a reduced net detrainment of ice cloud condensates and water vapor in this region. Since we expect a decrease in the upper-tropospheric dry static stability, on the grounds that the tropical temperature profile adheres to a moist adiabatic profile, the increase in the upper-tropospheric stability seen in our simulations near the tropopause may be a consequence of radiative heating by ozone (Harrop & Hartmann, 2012) or a result of the changes in the Brewer–Dobson circulation (Chae & Sherwood, 2010); a detailed investigation into the energy budget of the tropics and precipitation efficiency is out of the scope of this work.

Related to previous works (e.g., Ohno and Satoh (2018) and Gasparini et al. (2021)), we have found that the net depositional growth of ice cloud condensates plays a crucial role in controlling the tropical high cloud fraction, but we show that this is also the case when the tropical SSTs remain invariant. This is particularly relevant in the lower part of the tropical upper troposphere (between 8 and 10 km). Our results indicate that the relative importance of cloud microphysical processes over net convective detrainment is altitude-dependent. Although sedimentation of ice aggregates is found to dominate the microphysical tendency of q_{cf}, consistent with the study by Beydoun et al. (2021), we found that the microphysical *sources* of q_{cf}, such as the net depositional growth of ice aggregates (refer to figure 1 of Morrison et al. (2020)), and their influence on the ice cloud fraction in the tropical upper troposphere to be particularly significant. Heterogeneous and homogeneous ice nucleation processes have not been found to significantly affect the ice cloud fraction in our simulations, and secondary ice production processes were not considered.

The decrease in the net depositional growth of ice aggregates with extratropical warming is a consequence of reduced environmental water vapour in the tropical ascent

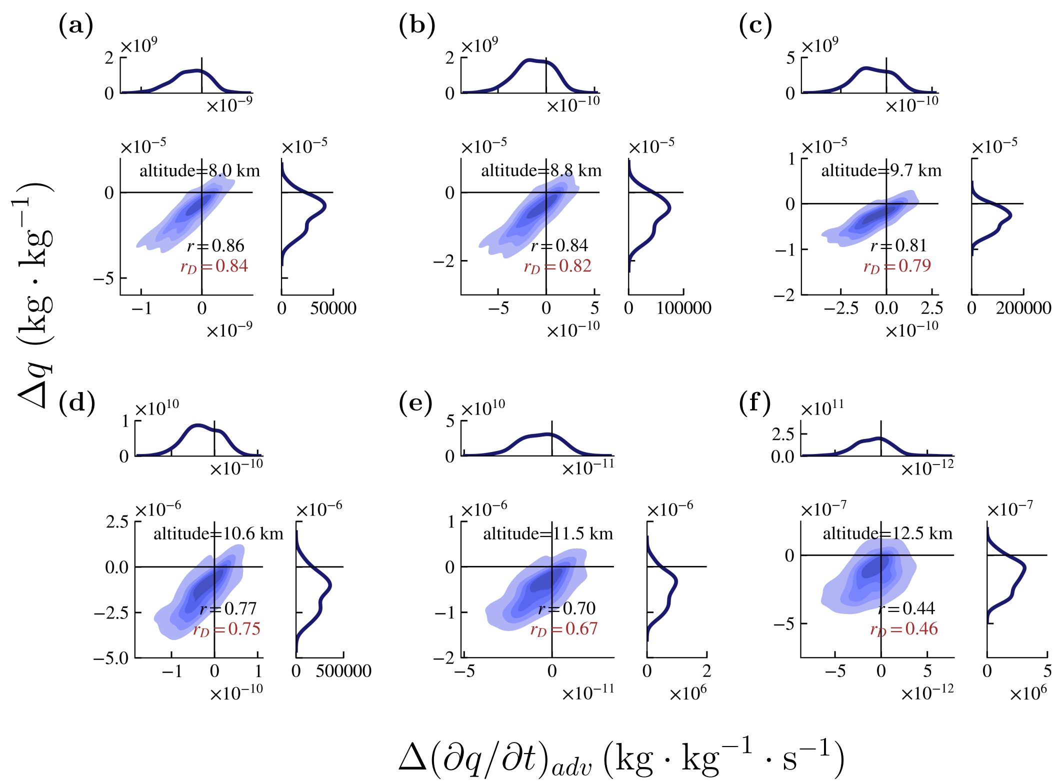

Figure 12: Kernel density estimates for the joint probability density function of the changes in specific humidity and its advective tendency ($\Delta(\partial q/\partial t)_{adv}$) are presented. The zonal- and annual means of the respective quantities are plotted, and the distance (r_D) and Pearson correlation coefficients (r) are computed, which increase as altitude decreases within the range studied. The reduction in the advective moistening tendency is evident across all considered altitudes.

region. The resolved large-scale vertical motion carries less moisture into the tropical upper troposphere (i.e., reduced mean vertical advection), resulting in a decreased specific humidity and relative humidity[5] in the region. There is also a decrease in the convectively detrained water vapor into the upper troposphere of the tropical ascent region. In reality, however, moisture is almost exclusively carried upwards within narrow cloudy updrafts in the tropical free-troposphere due to positive static stability. The large-scale mean upward transport of water vapor in the deep tropics is then a balance between relatively large upward transport within narrow updrafts and downward transport within the broad environment exhibiting weak subsidence. General Circulation Models (GCMs), on the other hand, partition this moisture transport into transport done by the convection scheme, for which the upward mass flux must be exactly compensated by subsidence within an individual grid cell and convective time step, and a large-scale resolved flow governed by pressure gradients resulting from grid-mean increments including warming from this convective parameterization step. This implies that there can be *ascent* in GCM-resolved flow, which therefore transports water vapor upward on average, while water

[5] Note the slight cooling of the free-troposphere with extratropical warming. The decrease in the relative humidity in the tropical upper troposphere is caused by a reduced moisture advected by the weakened large-scale circulation.

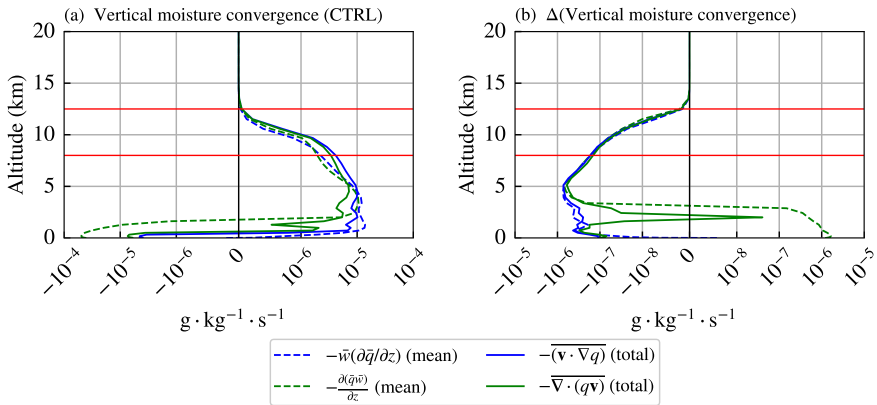

Figure 13: Vertical profiles of the vertical moisture convergence by the mean flow (green dashed) and the total moisture convergence (green solid) for the control simulation and their response to extratropical warming are shown in subfigures (a) and (b) respectively. The vertical and total advective terms of moisture are also plotted as blue dashed, and blue solid curves, respectively. The weakening of the mean vertical advection (blue dashed) dominates the reduction in the total moisture convergence (green solid), leading to a reduced moistening of the upper troposphere in the perturbed simulation. The detailed derivation of the decomposition of the total moisture flux convergence ($-\overline{\nabla \cdot (q\mathbf{v})}$) into contributions from the mean flow and transient eddies, which are again expressed as a sum of advective ($-\overline{\mathbf{v} \cdot \nabla q}$) and flow convergence ($-\overline{q(\nabla \cdot \mathbf{v})}$) terms, is given in Appendix A. Additional figures that illustrate the different decomposed terms are plotted in the supplementary (see figures S2, S3 and S4).

vapor in the real world (or in fine-grid explicit convection simulations) would be carried upward only in narrow convective updrafts. In our framework, pathway IIA (see figure 4) describes the interaction between GCM-resolved large-scale flow and the parameterized cloud microphysical processes (e.g., net depositional growth of ice cloud condensates), whereas pathway IIB describes the interaction between the parameterized convection and parameterized cloud microphysics.

The convective parameterization scheme and its impact on the large-scale environment may thus have implications on how the convective, advective and microphysical processes interact with one another in a GCM. Further investigations using either superparameterization schemes or cloud-resolving simulations may therefore be necessary to test the robustness of these results.

5 Data Availability Statement

Simulation data for the figures are archived at `https://doi.org/10.5281/zenodo.8273593` (Natchiar, 2023). We acknowledge the use of the following python libraries: Iris (Met Office, 2010 - 2013), pandas (McKinney et al., 2011), seaborn (Waskom, 2021), Matplotlib (Hunter, 2007), and aeolus (Sergeev & Zamyatina, 2023).

Appendix A Moisture convergence by the mean flow and transient eddies

The atmospheric water vapor budget can be written as $\partial q/\partial t + \nabla \cdot (q\mathbf{v}) = E - P$, where E and P are the local evaporation and precipitation rates respectively. Considering steady-state, we have

$$-\nabla \cdot (q\mathbf{v}) = P - E\,. \tag{A1}$$

This equation represents the equivalence between the local moisture flux convergence and the local net precipitation. Decomposing the specific humidity (q) and wind vector ($\mathbf{v}$) into mean and transient eddy components, we have

$$-\nabla \cdot (q\mathbf{v}) = -\nabla \cdot ((\bar{q} + q')(\bar{\mathbf{v}} + \mathbf{v}')) = -\nabla \cdot (\bar{q}\bar{v} + \bar{q}\mathbf{v}' + q'\bar{\mathbf{v}} + q'\mathbf{v}')\,. \tag{A2}$$

Here, overbar denotes the time-mean and the prime notation represents transient eddy components which are deviations of the quantities from their respective time-means. Taking the time-mean of the total moisture convergence term, we arrive at the Reynolds decomposition

$$-\overline{\nabla \cdot (q\mathbf{v})} = -\nabla \cdot (\bar{q}\bar{\mathbf{v}}) - \overline{\nabla \cdot q'\mathbf{v}'}\,, \tag{A3}$$

since by definition, the time-means of $\bar{q}\mathbf{v}'$ and $q'\bar{\mathbf{v}}$ are zero. Using the product rule of divergence, this becomes

$$-\overline{\nabla \cdot (q\mathbf{v})} = \underbrace{-\bar{q}(\nabla \cdot \bar{\mathbf{v}}) - \bar{\mathbf{v}} \cdot \nabla \bar{q}}_{\textbf{mean component}}\ \underbrace{-\overline{q'(\nabla \cdot \mathbf{v}')} - \overline{\mathbf{v}' \cdot \nabla q'}}_{\textbf{eddy component}}\,, \tag{A4}$$

Here, $-\bar{q}(\nabla \cdot \bar{\mathbf{v}})$ signifies the mean flow convergence weighted by the mean specific humidity, and $-\overline{q'(\nabla \cdot \mathbf{v}')}$ signifies the eddy flow convergence weighted by its respective specific humidity, while $-\bar{\mathbf{v}} \cdot \nabla \bar{q}$ and $-\overline{\mathbf{v}' \cdot \nabla q'}$ denote the respective advection of moisture by the mean and eddy flows. The above equation can be further decomposed into horizontal and vertical components as

$$\begin{aligned} -\overline{\nabla \cdot (q\mathbf{v})} = &- \bar{q}(\nabla_h \cdot \bar{\mathbf{v}}_h) - \bar{q}\frac{\partial \bar{w}}{\partial z} - \bar{\mathbf{v}}_h \cdot \nabla_h \bar{q} - \bar{w}\frac{\partial \bar{q}}{\partial z} \\ &- \overline{q'(\nabla \cdot \mathbf{v}'_h)} - \overline{q'\frac{\partial w'}{\partial z}} - \overline{\mathbf{v}'_h \cdot \nabla_h q'} - \overline{w'\frac{\partial q'}{\partial z}}\,, \end{aligned} \tag{A5}$$

where the wind vector $\mathbf{v} = (u, v, w)$ along the zonal (λ), meridional (ϕ) and vertical (z) directions. The subscript $_h$ denotes the corresponding horizontal component. The horizontal component of the divergence of a vector $\mathbf{A}$ is, for example, defined as

$$\nabla_h \cdot \mathbf{A}_h = \frac{1}{R\cos\phi}\left(\frac{\partial A_\lambda}{\partial \lambda} + \frac{\partial (A_\phi \cos\phi)}{\partial \phi}\right)\,, \tag{A6}$$

where A_λ and A_ϕ are the zonal and meridional components of the vector $\mathbf{A}$ and R is the radius of the Earth.

Appendix B Subsidence vertical velocity

The expression for the domain-mean subsidence velocity ($\bar{w}_{sub}$), derived from the dry static energy budget under the assumption of steady-state and weak temperature gradient (WTG) within the tropics, is given by (Jenney et al., 2020; Jeevanjee, 2022):

$$\bar{w}_{sub} = \frac{\bar{\mathcal{H}}_{rad} + \bar{\mathcal{H}}_e}{\Gamma_d - \Gamma}\,, \tag{B1}$$

where $\bar{\mathcal{H}}_{rad} = \bar{Q}_{rad}/C_p$ and $\bar{\mathcal{H}}_e = \bar{Q}_e/C_p$ denote the diabatic heating terms in K/s, representing radiative and evaporative cooling rates (i.e., $\bar{\mathcal{H}}_{rad} < 0\,, \bar{\mathcal{H}}_e < 0$), respectively, and Γ_d and Γ represent the dry and moist adiabatic lapse rates.

Appendix C Bulk updraft cloud model

The equations for the bulk updraft cloud model, following Yanai et al. (1973), are given as below.

Mass flux, M^P:

$$-\frac{\partial(M^P)}{\partial p} = E - N - D\,, \tag{C1}$$

Moisture flux:

$$-\frac{\partial(M^P\,q^P)}{\partial p} = Eq^E - Nq^N - Dq^R - Q\,, \tag{C2}$$

Sum of liquid and frozen condensate fluxes:

$$-\frac{\partial(M^P q^P_{cl} + M^P q^P_{cf})}{\partial p} = E(q^E_{cl} + q^E_{cf}) - N(q^N_{cl} + q^N_{cf}) - D(q^R_{cl} + q^R_{cf}) + Q - P\,. \tag{C3}$$

Here, the parcel mass flux is M^P in Pa/s; the entrainment rate, and the mixing and forced detrainment rates are defined in terms of the parcel mass flux as $E = \epsilon M^P\,, N = \mu M^P\,, D = \delta M^P$, where $\epsilon\,, \mu\,, \delta$ are the respective coefficients in Pa^{-1}; $q\,, q_{cl}\,, q_{cf}$ are the parcel specific humidity, cloud liquid condensate and cloud ice condensate amount in kg/(kg of air); Q denotes the conversion of water vapor into liquid water or ice; P denotes the precipitation fluxes of liquid and ice condensates. Note that the mean quantities over a gridbox are calculated by also accounting for processes occurring within the cloud environment.

Acknowledgments

SRMN is thankful to Ruth Geen, Ian Boutle and Mike Byrne for useful discussions. SRMN, FHL and GKV were supported by NERC CIRCULATES `NE/T006285/1`. MJW was supported by the Met Office Hadley Centre Climate Programme funded by DSIT. We acknowledge the use of Monsoon2 system, a collaborative facility supplied under the Joint Weather and Climate Research Programme, a strategic partnership between the Met Office and the Natural Environment Research Council, UK. DES was supported by a UKRI Future Leaders Fellowship `MR/T040866/1`.

References

Beydoun, H., Caldwell, P. M., Hannah, W. M., & Donahue, A. S. (2021). Dissecting anvil cloud response to sea surface warming. *Geophysical Research Letters*, *48*(15), e2021GL094049.

Bony, S., Stevens, B., Coppin, D., Becker, T., Reed, K. A., Voigt, A., & Medeiros, B. (2016). Thermodynamic control of anvil cloud amount. *Proceedings of the National Academy of Sciences*, *113*(32), 8927–8932.

Bordoni, S., & Schneider, T. (2008). Monsoons as eddy-mediated regime transitions of the tropical overturning circulation. *Nature Geoscience*, *1*(8), 515–519.

Boutle, I. A., Mayne, N. J., Drummond, B., Manners, J., Goyal, J., Lambert, F. H., & et al. (2017). Exploring the climate of Proxima b with the Met Office Unified Model. *Astronomy & Astrophysics*, *601*, A120.

Chae, J. H., & Sherwood, S. C. (2010). Insights into cloud-top height and dynamics from the seasonal cycle of cloud-top heights observed by misr in the west pacific region. *Journal of the atmospheric sciences*, *67*(1), 248–261.

Chaudhuri, A., & Hu, W. (2019). A fast algorithm for computing distance correlation. *Computational statistics & data analysis*, *135*, 15–24.

Chen, Y.-W., Seiki, T., Kodama, C., Satoh, M., Noda, A. T., & Yamada, Y. (2016). High cloud responses to global warming simulated by two different cloud microphysics schemes implemented in the Nonhydrostatic Icosahedral Atmospheric Model (NICAM). *Journal of Climate*, *29*(16), 5949–5964.

Davy, R., Chen, L., & Hanna, E. (2018). Arctic amplification metrics. *International Journal of Climatology*, *38*(12), 4384–4394.

Derbyshire, S., Maidens, A., Milton, S., Stratton, R., & Willett, M. (2011). Adaptive detrainment in a convective parametrization. *Quarterly Journal of the Royal Meteorological Society*, *137*(660), 1856–1871.

Field, P. R., Heymsfield, A. J., & Bansemer, A. (2007). Snow size distribution parameterization for midlatitude and tropical ice clouds. *Journal of the Atmospheric Sciences*, *64*(12), 4346–4365.

Gasparini, B., Rasch, P. J., Hartmann, D. L., Wall, C. J., & Duetsch, M. (2021). A lagrangian perspective on tropical anvil cloud lifecycle in present and future climate. *Journal of Geophysical Research: Atmospheres*, *126*(4), e2020JD033487.

Gregory, D., & Rowntree, P. (1990). A mass flux convection scheme with representation of cloud ensemble characteristics and stability-dependent closure. *Monthly Weather Review*, *118*(7), 1483–1506.

Harrison, E. F., Minnis, P., Barkstrom, B., Ramanathan, V., Cess, R., & Gibson, G. (1990). Seasonal variation of cloud radiative forcing derived from the Earth Radiation Budget Experiment. *Journal of Geophysical Research: Atmospheres*, *95*(D11), 18687–18703.

Harrop, B. E., & Hartmann, D. L. (2012). Testing the role of radiation in determining tropical cloud-top temperature. *Journal of Climate*, *25*(17), 5731–5747.

Hartmann, D. L., & Berry, S. E. (2017). The balanced radiative effect of tropical anvil clouds. *Journal of Geophysical Research: Atmospheres*, *122*(9), 5003–5020.

Hartmann, D. L., & Larson, K. (2002). An important constraint on tropical cloud-climate feedback. *Geophysical research letters*, *29*(20), 12–1.

Holland, M. M., & Bitz, C. M. (2003). Polar amplification of climate change in coupled models. *Climate dynamics*, *21*(3-4), 221–232.

Hunter, J. D. (2007). Matplotlib: A 2D Graphics Environment. *Computing in Science & Engineering*, *9*(3), 90–95. Retrieved from `http://ieeexplore.ieee.org/document/4160265/` doi: 10.1109/MCSE.2007.55

Jeevanjee, N. (2022). Three rules for the decrease of tropical convection with global warming. *Journal of Advances in Modeling Earth Systems*, *14*(11), e2022MS003285.

Jenney, A. M., Randall, D. A., & Branson, M. (2020). Understanding the response of tropical ascent to warming using an energy balance framework. *Journal of Advances in Modeling Earth Systems*, *12*(6), e2020MS002056.

Kim, D., Kim, H., Kang, S. M., Stuecker, M. F., & Merlis, T. M. (2022). Weak hadley cell intensity changes due to compensating effects of tropical and extratropical radiative forcing. *npj Climate and Atmospheric Science*, *5*(1), 61.

Knutson, T. R., & Manabe, S. (1995). Time-mean response over the tropical pacific to increased c02 in a coupled ocean-atmosphere model. *Journal of Climate*, *8*(9), 2181–2199.

Kuang, Z., & Hartmann, D. L. (2007). Testing the fixed anvil temperature hypothesis in a cloud-resolving model. *Journal of Climate*, *20*(10), 2051–2057.

Manabe, S., & Stouffer, R. J. (1980). Sensitivity of a global climate model to an increase of CO2 concentration in the atmosphere. *Journal of Geophysical Research: Oceans*, *85*(C10), 5529–5554.

McKinney, W., et al. (2011). pandas: a foundational python library for data analysis and statistics. *Python for high performance and scientific computing*, *14*(9), 1–9.

Met Office. (2010 - 2013). Iris: A python package for analysing and visualising meteorological and oceanographic data sets (v1.2 ed.) [Computer software manual]. Exeter, Devon. Retrieved from `http://scitools.org.uk/`

Morrison, H., van Lier-Walqui, M., Fridlind, A. M., Grabowski, W. W., Harrington, J. Y., Hoose, C., & et al. (2020). Confronting the challenge of modeling cloud and precipitation microphysics. *Journal of advances in modeling earth systems*, *12*(8), e2019MS001689.

Natchiar, S. M. (2023, August). *Reduction in the Tropical High Cloud Fraction in Response to an Indirect Weakening of the Hadley Cell.* Zenodo. Retrieved from `https://doi.org/10.5281/zenodo.8273593` doi: 10.5281/zenodo.8273593

Ohno, T., & Satoh, M. (2018). Roles of cloud microphysics on cloud responses to sea surface temperatures in radiative-convective equilibrium experiments using a high-resolution global nonhydrostatic model. *Journal of Advances in Modeling Earth Systems*, *10*(8), 1970–1989.

Ohno, T., Satoh, M., & Noda, A. (2019). Fine vertical resolution radiative-convective equilibrium experiments: Roles of turbulent mixing on the high-cloud response to sea surface temperatures. *Journal of Advances in Modeling Earth Systems*, *11*(6), 1637–1654.

Ramanathan, V., Cess, R., Harrison, E., Minnis, P., Barkstrom, B., Ahmad, E., & Hartmann, D. (1989). Cloud-radiative forcing and climate: Results from the Earth Radiation Budget Experiment. *Science*, *243*(4887), 57–63.

Saint-Lu, M., Bony, S., & Dufresne, J.-L. (2020). Observational evidence for a stability iris effect in the tropics. *Geophysical Research Letters*, *47*(14), e2020GL089059.

Schiro, K. A., Su, H., Wang, Y., Langenbrunner, B., Jiang, J. H., & Neelin, J. D. (2019). Relationships between tropical ascent and high cloud fraction changes with warming revealed by perturbation physics experiments in CAM5. *Geophysical Research Letters*, *46*(16), 10112–10121.

Seeley, J. T., Jeevanjee, N., Langhans, W., & Romps, D. M. (2019). Formation of tropical anvil clouds by slow evaporation. *Geophysical Research Letters*, *46*(1), 492–501.

Sergeev, D. E., & Zamyatina, M. (2023, April). *aeolus.* Zenodo. Retrieved from `https://doi.org/10.5281/zenodo.7829974` doi: 10.5281/zenodo.7829974

Sherwood, S., Webb, M. J., Annan, J. D., Armour, K. C., Forster, P. M., Hargreaves, J. C., & et al. (2020). An assessment of earth's climate sensitivity using multiple lines of evidence. *Reviews of Geophysics*, *58*(4), e2019RG000678.

Singh, M. S., & Kuang, Z. (2016). Exploring the role of eddy momentum fluxes in determining the characteristics of the equinoctial hadley circulation: Fixed-sst simulations. *Journal of the Atmospheric Sciences*, *73*(6), 2427–2444.

Singh, M. S., Kuang, Z., & Tian, Y. (2017). Eddy influences on the strength of the hadley circulation: Dynamic and thermodynamic perspectives. *Journal of the Atmospheric Sciences*, *74*(2), 467–486.

Singh, M. S., & O'Gorman, P. A. (2015). Increases in moist-convective updraught velocities with warming in radiative-convective equilibrium. *Quarterly Journal*

of the Royal Meteorological Society, *141*(692), 2828–2838.
Smith, R. (1990). A scheme for predicting layer clouds and their water content in a general circulation model. *Quarterly Journal of the Royal Meteorological Society*, *116*(492), 435–460.
Stauffer, C. L., & Wing, A. A. (2022). Properties, changes, and controls of deep-convecting clouds in radiative-convective equilibrium. *Journal of Advances in Modeling Earth Systems*, *14*(6), e2021MS002917.
Székely, G. J., Rizzo, M. L., & Bakirov, N. K. (2007). Measuring and testing dependence by correlation of distances.
Tsushima, Y., Iga, S.-i., Tomita, H., Satoh, M., Noda, A. T., & Webb, M. J. (2014). High cloud increase in a perturbed SST experiment with a global nonhydrostatic model including explicit convective processes. *Journal of Advances in Modeling Earth Systems*, *6*(3), 571–585.
Walters, D., Baran, A. J., Boutle, I., Brooks, M., Earnshaw, P., Edwards, J., & et al. (2019). The Met Office Unified Model global atmosphere 7.0/7.1 and JULES global land 7.0 configurations. *Geoscientific Model Development*, *12*(5), 1909–1963.
Waskom, M. L. (2021). seaborn: statistical data visualization. *Journal of Open Source Software*, *6*(60), 3021. Retrieved from `https://doi.org/10.21105/joss.03021` doi: 10.21105/joss.03021
Wilson, D. R., & Ballard, S. P. (1999). A microphysically based precipitation scheme for the uk meteorological office unified model. *Quarterly Journal of the Royal Meteorological Society*, *125*(557), 1607–1636.
Wilson, D. R., Bushell, A. C., Kerr-Munslow, A. M., Price, J. D., & Morcrette, C. J. (2008). PC2: A prognostic cloud fraction and condensation scheme. I: Scheme description. *Quarterly Journal of the Royal Meteorological Society: A journal of the atmospheric sciences, applied meteorology and physical oceanography*, *134*(637), 2093–2107.
Wing, A. A., Stauffer, C. L., Becker, T., Reed, K. A., Ahn, M.-S., Arnold, N. P., & et al. (2020). Clouds and convective self-aggregation in a multimodel ensemble of radiative-convective equilibrium simulations. *Journal of Advances in Modeling Earth Systems*, *12*(9), e2020MS002138.
Yanai, M., Esbensen, S., & Chu, J.-H. (1973). Determination of bulk properties of tropical cloud clusters from large-scale heat and moisture budgets. *Journal of Atmospheric Sciences*, *30*(4), 611–627.
Zelinka, M. D., & Hartmann, D. L. (2010). Why is longwave cloud feedback positive? *Journal of Geophysical Research: Atmospheres*, *115*(D16).
Zelinka, M. D., & Hartmann, D. L. (2011). The observed sensitivity of high clouds to mean surface temperature anomalies in the tropics. *Journal of Geophysical Research: Atmospheres*, *116*(D23).

Supporting Information for "Reduction in the Tropical High Cloud Fraction in Response to an Indirect Weakening of the Hadley Cell"

S. R. Monisha Natchiar[1], Mark J Webb[2], F Hugo Lambert[1], Geoffrey K Vallis[1], Cyril J Morcrette[1,2], Christopher E. Holloway[3], Denis E. Sergeev[4]

[1]Department of Mathematics and Statistics, University of Exeter, Exeter EX4 4QE, UK

[2]Met Office, FitzRoy Road, Exeter EX1 3PB, UK

[3]Department of Meteorology, University of Reading, Reading RG6 6BB, UK

[4]Department of Physics and Astronomy, University of Exeter, Exeter, EX4 4QL, UK

Contents of this file

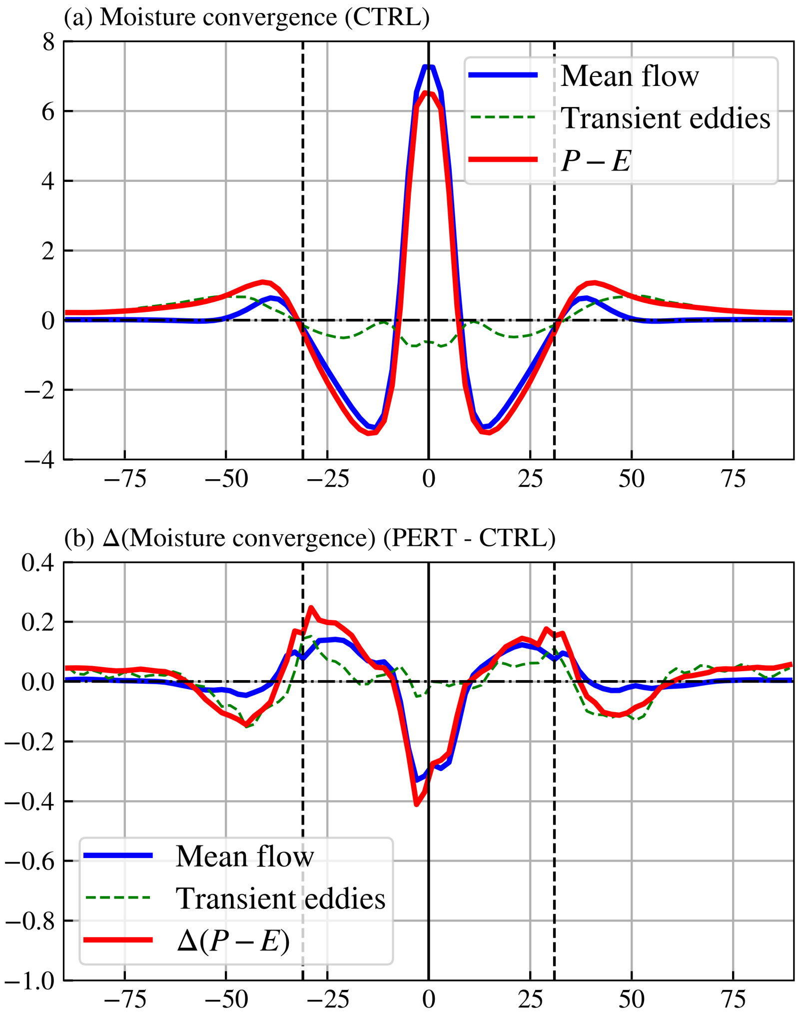

Figure S1. Moisture convergence by the mean flow and the transient eddies in the control simulation with PC2 cloud scheme and GR mass-flux convection scheme is plotted in (a), while the difference in moisture convergence between the perturbed and control simulations is plotted in (b) that shows a decrease in the mean moisture convergence in the deep tropics. The vertically integrated moisture convergence by the mean flow is computed as $\nabla_h \cdot \int_0^{z_t} \bar{\rho}\bar{q}\bar{\mathbf{v}}_h \, \mathrm{d}z$, where $\bar{\mathbf{v}}_h$ is the time-mean horizontal velocity vector, $\bar{q}$ is the time-mean specific humidity, and z_t denotes the top-of-atmosphere height. Similarly, the moisture convergence by the transient eddies is given by $\nabla_h \cdot \int_0^{z_t} \bar{\rho}\overline{q'\mathbf{v}'_h} \, \mathrm{d}z$, where prime ($'$) denotes the respective transient eddy quantities. Note that $P - E$ approximately balances the sum of moisture convergence terms due to the mean flow and transient eddies.

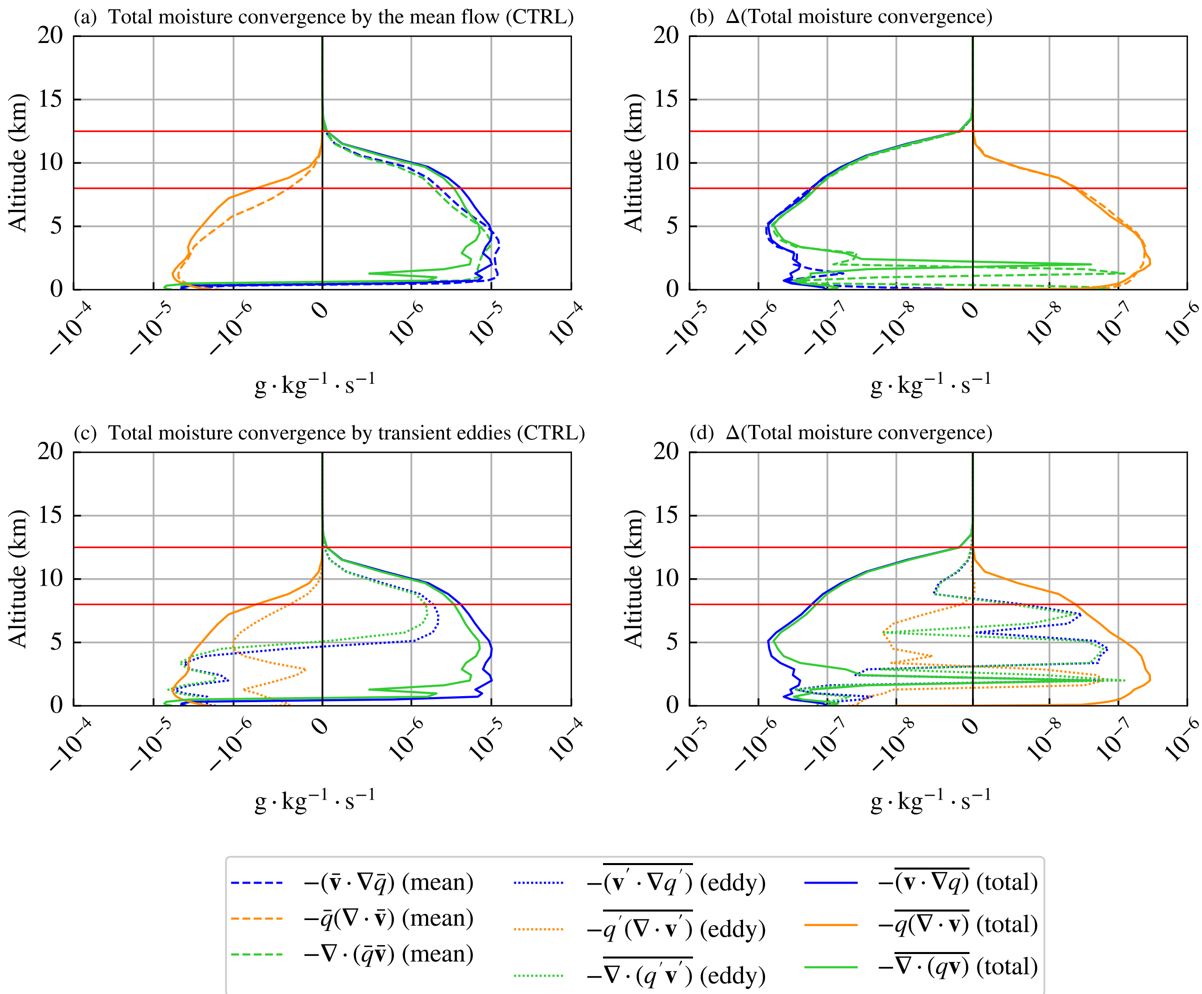

Figure S2. Moisture convergence by the mean flow (dashed curves) in the control simulation is shown in (a) and their response to extratropical warming is shown in (b). Similarly, the moisture convergence by the transient eddies (dotted curves) in the control is shown in (c) and their response in (d). Both simulations are run with the PC2 cloud scheme and GR mass-flux convection scheme. The solid curves indicate the total moisture convergence given by the sum of mean flow and transient eddy terms. The moisture convergence by the mean flow and transient eddies are further decomposed into advection (blue) and flow convergence terms (orange), with their sum represented by green curves. See Appendix A for more details on the derivation. The region of investigation is bounded by horizontal solid red lines; each of the terms plotted are averaged quantities over the tropical ascent region.

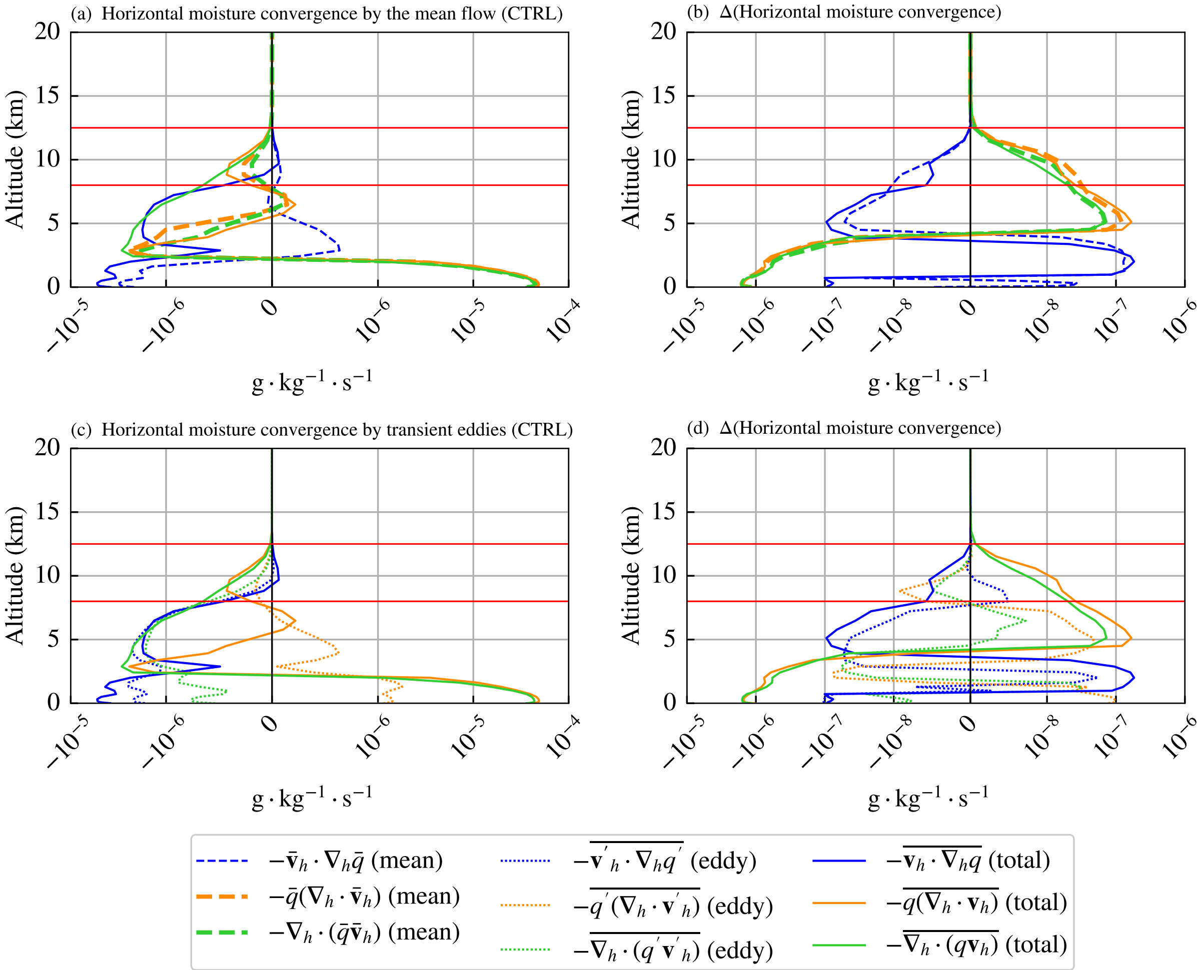

Figure S3. As in figure S2, but for the horizontal moisture convergence terms by the mean flow (dashed curves) in (a) and their response in (b), with the transient eddy components (dotted curves) in the control and the response plotted in (c) and (d), respectively. Note that while the horizontal moisture convergence predominantly influences the boundary layer transport of moisture, it does not contribute significantly to the upper-tropospheric moisture convergence, in comparison to vertical moisture convergence.

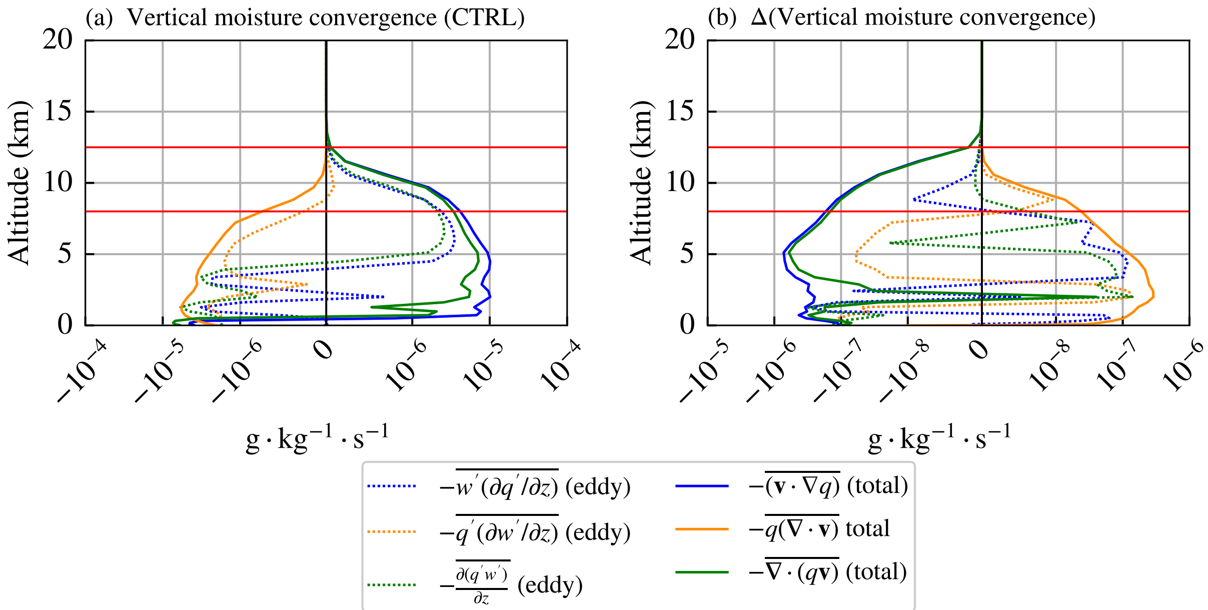

Figure S4. Vertical moisture convergence by the transient eddies (dotted curves) and the total moisture convergence terms (solid curves) are plotted in the control simulation in (a) and their response to extratropical warming in (b). Although transient eddies transport moisture into the deep tropics via vertical advection in the control, their response to extratropical warming is not significant in the region of interest compared to the changes in the mean vertical advection of moisture.

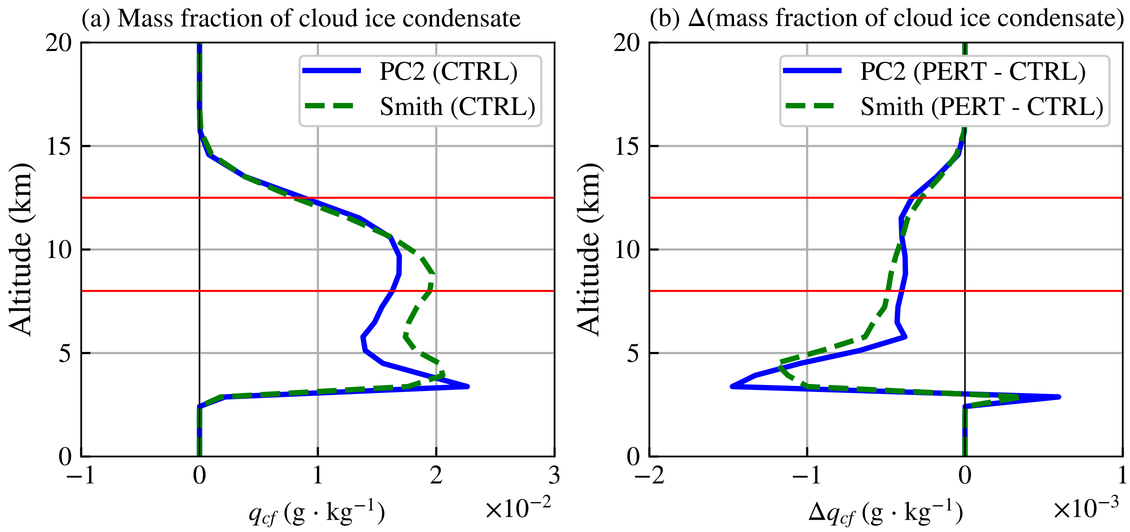

Figure S5. Vertical profiles of the mass fraction of ice cloud condensates (q_{cf}) in the control simulations (a) and the response to extratropical surface warming (b) are shown for both prognostic and diagnostic cloud schemes in the tropical ascent region. Both cloud schemes show a reduction in the ice cloud condensate amounts in the tropical ascent region. Red lines demarcate the region of interest (i.e., tropical upper-troposphere).

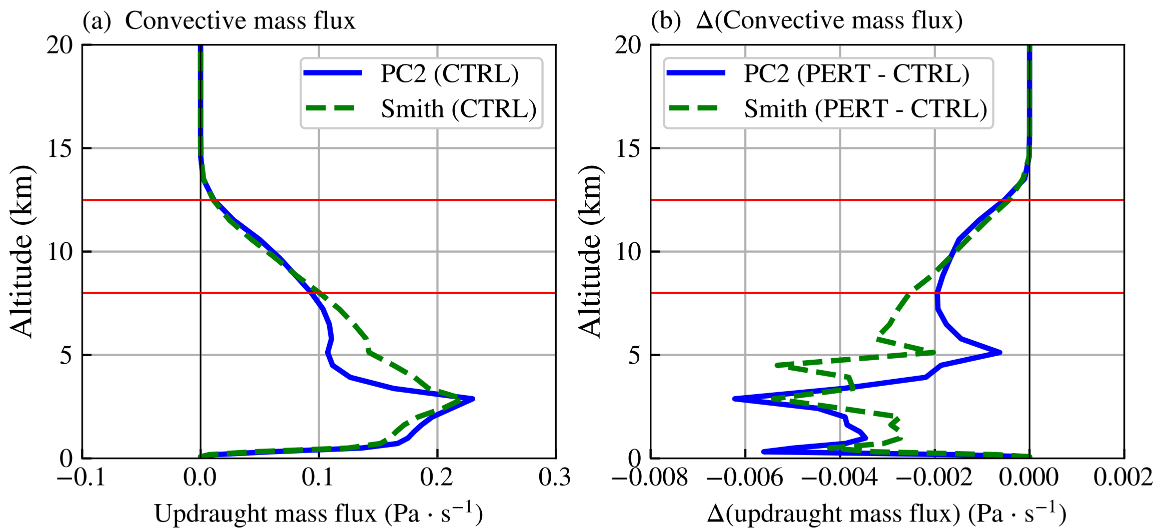

Figure S6. Vertical profiles of the updraft mass flux in the control simulation (a) and the response to extratropical warming (b) are plotted for two different cloud schemes. A decrease in the convective mass flux occurs as a result of a weakened Hadley circulation as is expected.

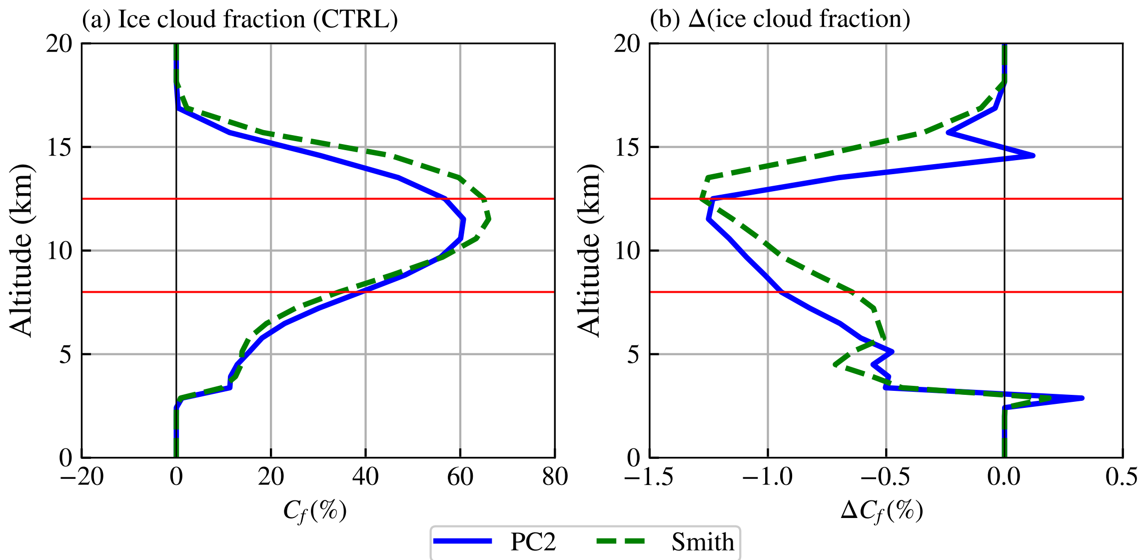

Figure S7. Vertical profiles of the ice cloud fraction (C_f) in the control simulation (a) and the difference between perturbed and control simulations (b) are plotted for two different cloud schemes. A maximum decrease in the ice cloud fraction of at least 1% can be observed at around 11.5 km where the ice cloud fraction peaks in the control simulation.

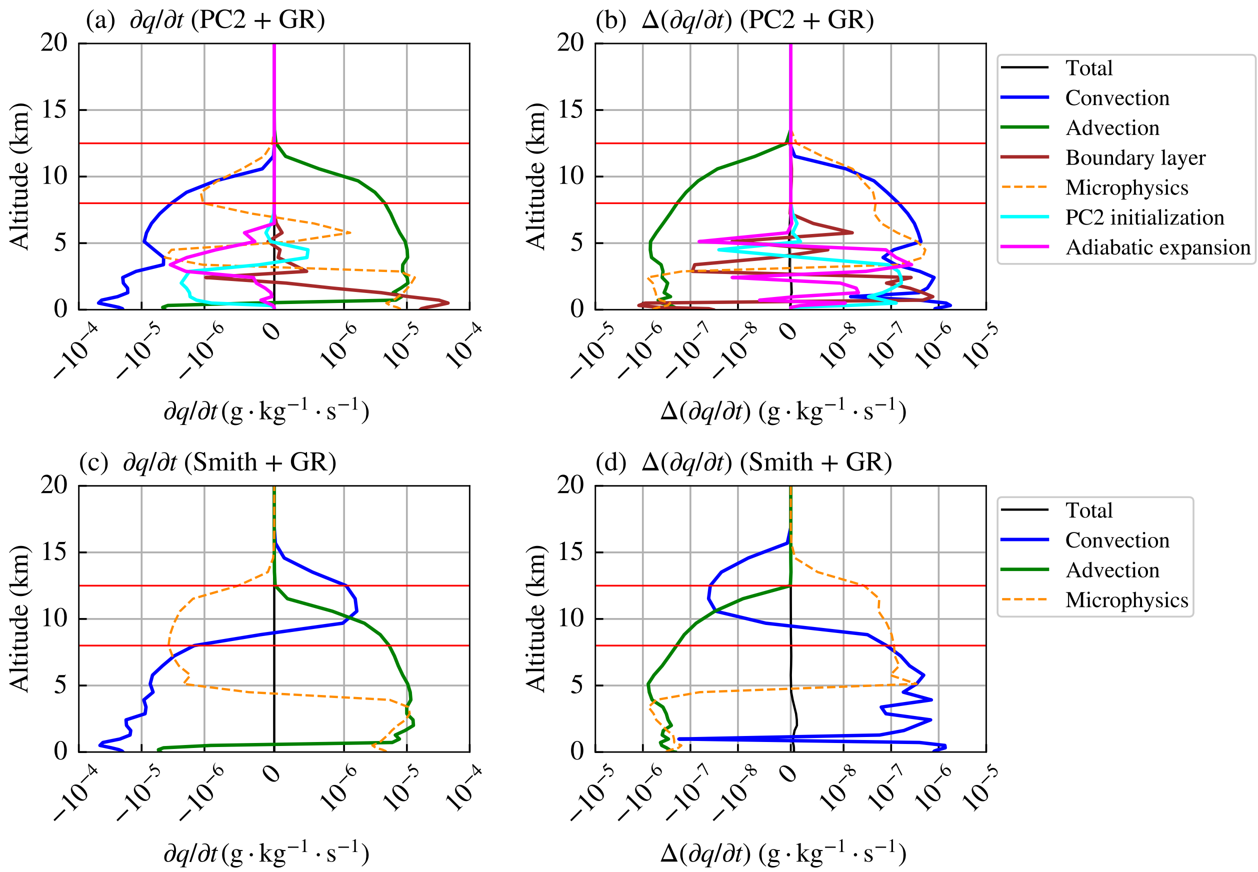

Figure S8. Vertical profiles of specific humidity tendencies in the control simulation (a, c) and their responses to extratropical warming (b, d) are plotted for both the prognostic (a, b) and diagnostic cloud schemes (c, d). A decrease in the advective tendency of specific humidity can be observed for both the cloud schemes (green curves), leading to reduced water vapor in the upper troposphere of the tropical ascent region. Note that the convectively detrained cloud condensates are evaporated in the diagnostic (Smith) cloud scheme resulting in a convective source of water vapor in the deep tropical upper troposphere (blue curve in (c)).

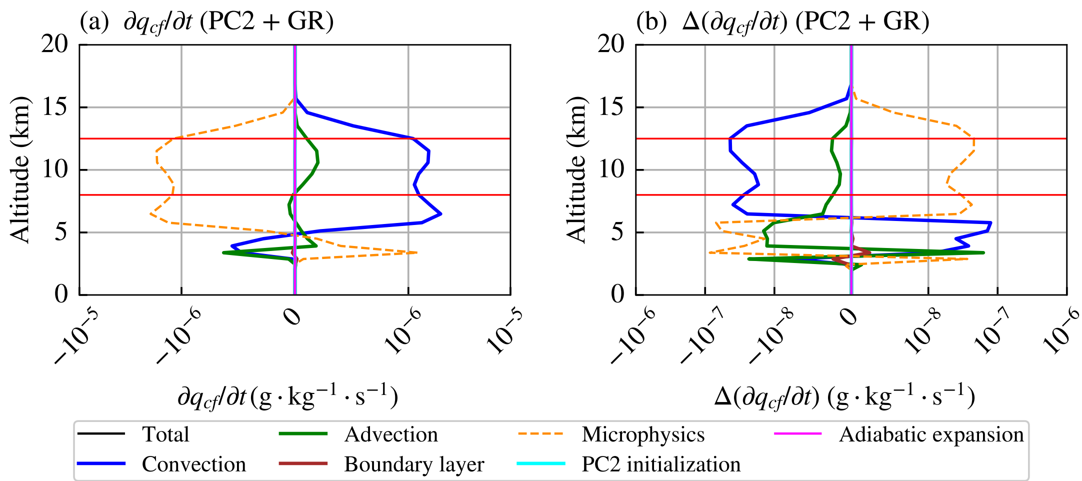

Figure S9. Vertical profiles of the tendencies of mass fraction of ice cloud condensates in the control simulation (a) and their responses to extratropical warming (b) are plotted for the PC2 (prognostic) cloud scheme with the GR mass-flux convection scheme. A decrease in the convective tendency of q_{cf} corresponds to a decrease in the updraft mass flux (M) in the tropical ascent region. The decrease in the microphysical tendency of ice cloud condensates (orange dashed curve in (b)) corresponds to a decrease in the sedimentation sink of ice aggregates, owing to the decrease in ice cloud fraction with extratropical warming.

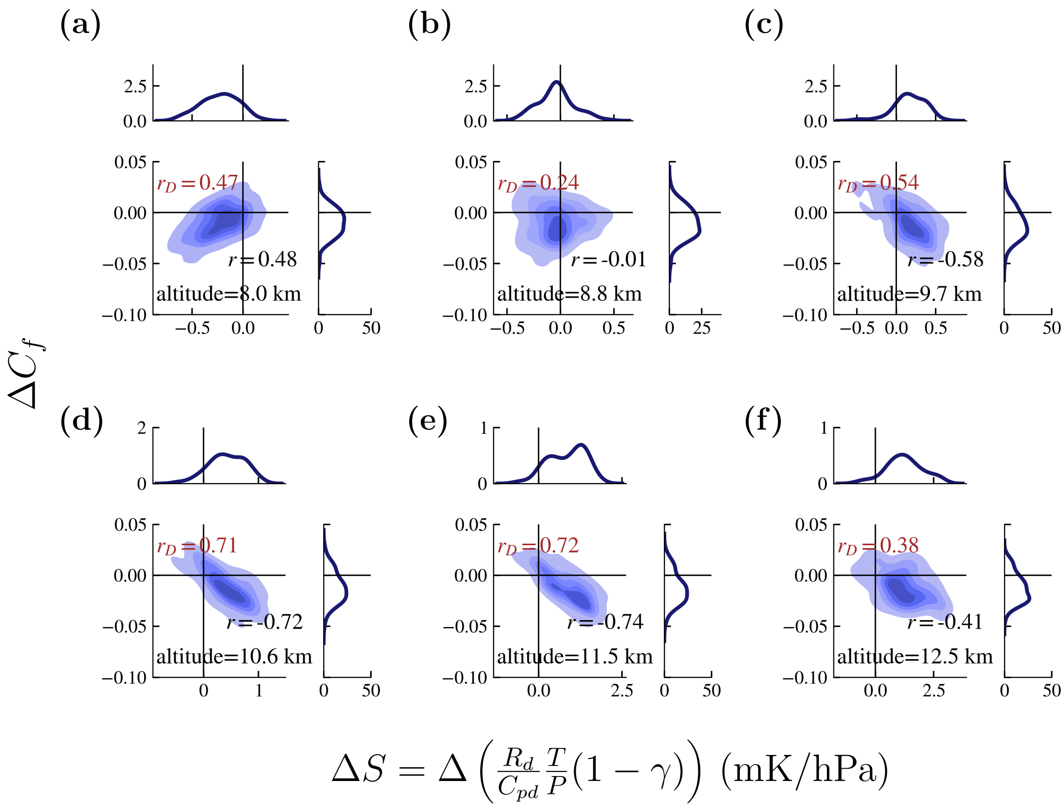

Figure S10. Kernel density estimates for the joint probability density function of changes in ice cloud fraction (ΔC_f) and dry static stability (ΔS), where $S = \frac{R_d}{C_{pd}} \frac{T}{P}(1 - \gamma)$, are presented. The zonal- and annual means of the respective quantities are plotted, and the Pearson (r) and distance correlation coefficient (r_D) are computed. The figure shows an increase in the dry static stability with altitude as a result of extratropical warming, albeit the altitude at which clouds detrain remaining relatively unchanged in the perturbed simulations. Note that the changes in the dry static stability are dominated by the changes in $(1 - \gamma)$ as shown in figure S11.

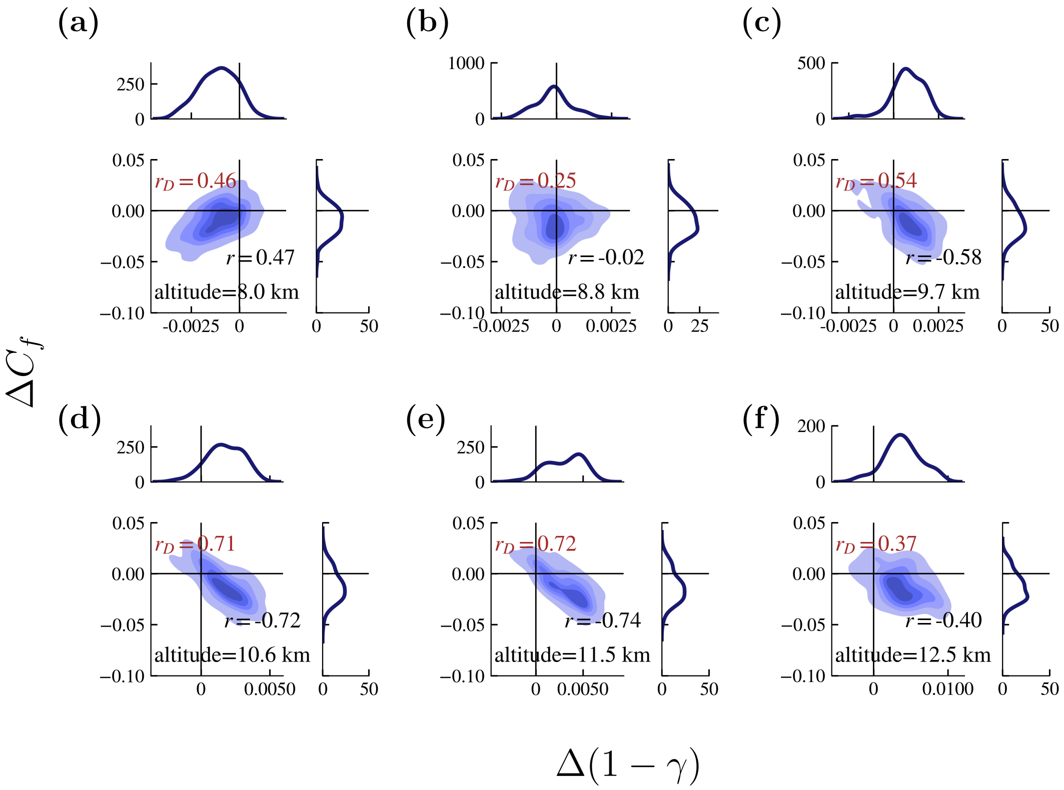

Figure S11. Kernel density estimates for the joint probability density function of changes in ice cloud fraction and $(1-\gamma)$ are presented. Here, $\gamma = \Gamma/\Gamma_d$ is the ratio of the moist to the dry adiabatic lapse rates. The zonal- and annual means of the respective quantities are plotted, and the Pearson (r) and distance correlation coefficient (r_D) are computed. The increase in static stability with altitude corresponds to an increase in $(1-\gamma)$ or a decrease in the moist adiabatic lapse rate $(\Gamma = -(\partial T/\partial z))$.

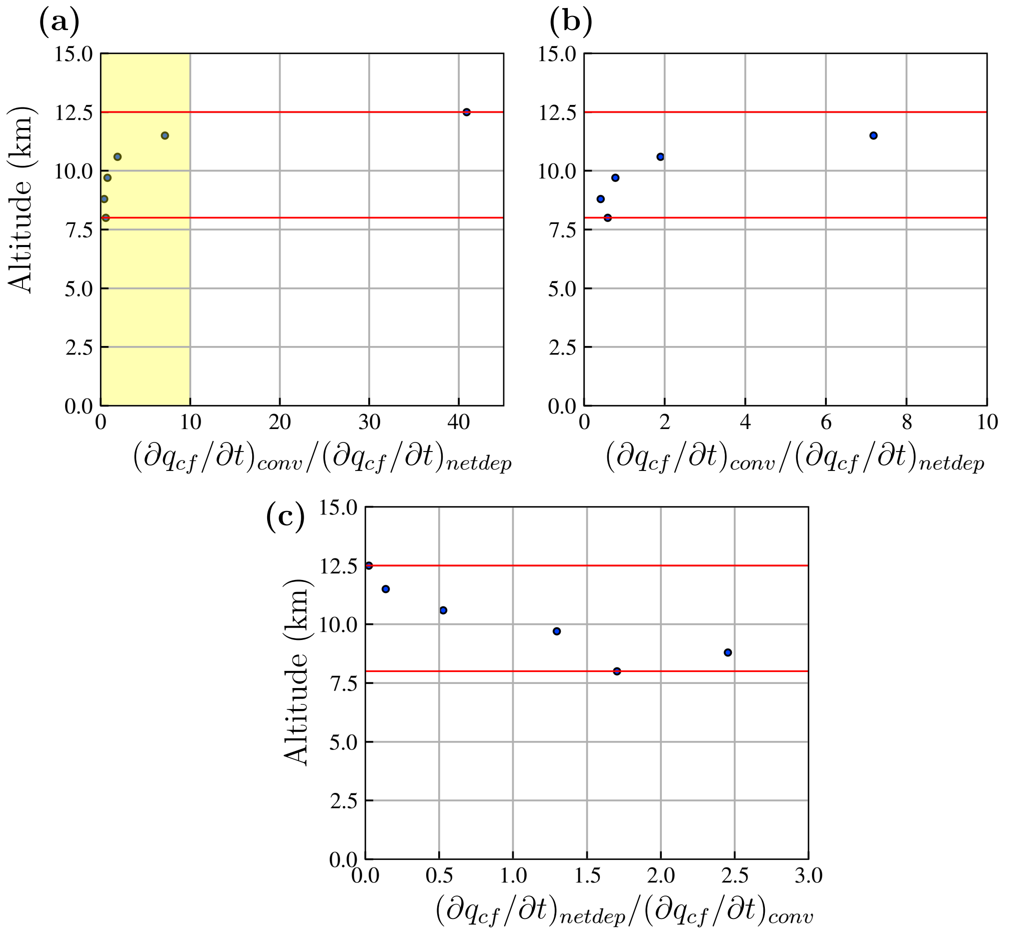

Figure S12. Ratio (a,b) and inverse ratio (c) of the convective tendency of mass fraction of cloud ice $((\frac{\partial q_{cf}}{\partial t})_{conv})$ to its net depositional tendency $(((\frac{\partial q_{cf}}{\partial t})_{netdep})$ are plotted. The subfigure (a) shows the leading-order influence of net convective detrainment in controlling ice cloud condensates and therefore ice cloud fraction near the peak net detrainment region (above 10 km). The shaded portion (in yellow) in subfigure (a) is shown on a different horizontal scale in (b), and along with subfigure (c) clearly depicts the importance of net depositional growth of ice cloud condensates over its convective tendency between the altitude range of 8 to 10 km. Annual and zonal-mean quantities averaged over the tropical ascent region over a period of 15 simulation years are plotted.